

UNIVERZITA KOMENSKÉHO V BRATISLAVE  
FAKULTA MATEMATIKY, FYZIKY A INFORMATIKY

CURRENT-PHASE RELATIONSHIP OF  
SUPERCONDUCTING QUANTUM DEVICES  
DIPLOMA THESIS

2023  
Bc. DANIEL BOBOK

UNIVERZITA KOMENSKÉHO V BRATISLAVE  
FAKULTA MATEMATIKY, FYZIKY A INFORMATIKY

CURRENT-PHASE RELATIONSHIP OF  
SUPERCONDUCTING QUANTUM DEVICES  
DIPLOMA THESIS

Študijný program: fyzika tuhých látok  
(Jednoodborové štúdium, magisterský II. st., denná forma)  
Študijný odbor: fyzika  
Školiace pracovisko: FMFI.KEF - Katedra experimentálnej fyziky  
Školiteľ: prof. RNDr. Miroslav Grajcar, DrSc.  
Konzultant: Mgr. Pavol Neilinger, PhD.

Bratislava, 2023  
Bc. Daniel Bobok



Univerzita Komenského v Bratislavе  
Fakulta matematiky, fyziky a informatiky

## ZADANIE ZÁVEREČNEJ PRÁCE

**Meno a priezvisko študenta:** Bc. Daniel Bobok  
**Študijný program:** fyzika tuhých látok (Jednooborové štúdium, magisterský II.  
st., denná forma)  
**Študijný odbor:** fyzika  
**Typ záverečnej práce:** diplomová  
**Jazyk záverečnej práce:** slovenský  
**Sekundárny jazyk:** anglický

**Názov:** Prúdovo-fázové charakteristiky supravodivých kvantových súčiastok  
*Current-phase relationship of superconducting quantum devices*

**Anotácia:** V rámci diplomovej práce sa študent naučí merať supravodivé kvantové  
súčiastky v nízkych teplotách. Dobuduje experimentálnu aparatúru, založenú  
na kryogénnom zosilňovači, ktorú navrhol a analyzoval počas bakalárskej  
práce.

**Ciel:** Cieľom je meranie prúdovo-fázových charakteristík Josephsonových spojov  
na báze topologických materiálov.

**Vedúci:** prof. RNDr. Miroslav Grajcar, DrSc.

**Konzultant:** Mgr. Pavol Neilinger, PhD.

**Katedra:** FMFI.KEF - Katedra experimentálnej fyziky

**Vedúci katedry:** prof. Dr. Štefan Matejčík, DrSc.

**Spôsob sprístupnenia elektronickej verzie práce:**

bez obmedzenia

**Dátum zadania:** 20.09.2021

**Dátum schválenia:** 21.09.2021

prof. RNDr. Peter Kúš, DrSc.

garant študijného programu

.....  
študent

.....  
vedúci práce

**Čestné prehlásenie:** Čestne prehlasujem, že som túto diplomovú prácu vypracoval samostatne s použitím uvedených zdrojov.

.....  
Daniel Bobok

**Pod'akovanie:** Chcem pod'akovať môjmu školiteľovi prof.RNDr. Miroslavovi Gráčaroví,DrSc. za trpezlivosť a usmernenie pri písaní tejto práce. Taktiež môjmu konzultantom Mgr. Pavlovi Neilingerovi, PhD. pri pomoci s dizajnom a úpravami zariadenia, Mgr.Samuelovi Kernovi za trpezlivosť a pomoc s tvorbou meracieho zariadenia a meraním, Mgr. Martinovi Baránkovi za pomoc s meraniami a Ing. Danielovi Mancovi za výrobu medených krabičiek. Najväčšia vďaka patrí mojej priateľke ktorá ma nepresta-jne podporovala a stála pri mne v najťažších chvíľach počas písania. A nakoniec tiež za skvelé vynálezy umelej inteligencie ChatGpt a Grammarly, ktoré mi pomohli pri preklade a kontrole pravopisu.

## Abstract

In this work, we focused on measuring Josephson junctions with the vision of measuring topological Josephson junctions in the future. We used a non-contact method of magnetic coupling of a parallel LC circuit to a quantum interferometer rf-SQUID for measurement. By coupling the rf-SQUID to the LC circuit, the resonance frequency shifts, which we were able to measure. We showed how the superconducting current in the rf-SQUID depends on the phase shift of the driving voltage and the current on the LC circuit, which we then demonstrated on an NbN nanobridge Josephson junction. The measured dependence was a sloped sinusoid compared to the ideal Josephson effect. The results of this work could be used for the development of one photon detector, and also for the development of SQUID fabrication technology.

**Keywords:** superconductivity, Josephson effect, cryogenic amplifiers, rf-SQUID, NbN

## Abstrakt

V tejto práci sme sa venovali meraniu josephsonových spojov s cieľom do budúcnosti merať topologické josephsonove spoje. Na meranie sme použili bezkontaktnú metódu magnetického naviazania paralelného LC ovodu na kvantový interferometer rf-SQUID. Meraním posunu rezonančnej frekvencie sme určili závislosť supravodivého prúdu v rf-SQUIDe od budiaceho magnetického toku. Meranie sme realizovali na NbN nanomostíkovom Josephsonovom spoji zapojeného do prstenca. Namerané prúdovo-fázove charakteristiky sme porovnali s rôznymi teoretickými modelmi. Výsledky tejto práce môžu byť použité pri zostrojovaní jedno-fotónového detektora ako pre vývoj technológie výroby rf-SQUIDov.

**Kľúčové slová:** supravodivosť, Josephsonov jav, kryogénne zosilňovače, rf-SQUID, NbN

# Contents

<b>1</b>	<b>Introduction</b>	<b>1</b>
<b>2</b>	<b>Theory</b>	<b>3</b>
2.1	Superconductivity . . . . .	3
2.2	Ginzburg-Landau order parameter and phase . . . . .	5
2.2.1	Ginzbur-Landau Coherence Length . . . . .	6
2.3	BCS . . . . .	8
2.3.1	Cooper pairs . . . . .	8
2.3.2	The BCS ground state . . . . .	10
2.3.3	Energy gap . . . . .	12
2.3.4	Coherence length . . . . .	13
2.4	Josephson effect . . . . .	14
2.4.1	Josephson junctions . . . . .	14
2.4.2	Quantum Josephson effect of tunnel junction . . . . .	15
2.5	Normal Metal And Constriction Junctions . . . . .	18
2.5.1	Andreev reflection . . . . .	18
2.5.2	Andreev bound states . . . . .	20
2.5.3	Current-Phase Relationship . . . . .	22
2.5.4	Short Junctions In Dirty Limit . . . . .	22
2.5.5	Dayem nanobridges . . . . .	23
<b>3</b>	<b>Current-phase relationship</b>	<b>25</b>
3.1	Magnetic Flux In The Superconducting Loop . . . . .	25
3.2	Magnetic Flux In The rf-SQUID . . . . .	26
3.2.1	Screening Effect . . . . .	27
3.3	Majorana bound states detection . . . . .	27
<b>4</b>	<b>Apparatus</b>	<b>29</b>
4.1	Refrigerator . . . . .	30
4.1.1	Pulse Tube . . . . .	30
4.1.2	$^3\text{He}$ pot . . . . .	31

4.1.3	Refrigerator Assembly . . . . .	31
4.2	Amplifier . . . . .	32
4.2.1	Thermal Noise . . . . .	32
4.2.2	Amplifier Noise . . . . .	33
4.2.3	Amplifier Design, Construction, and Test . . . . .	35
4.3	Tank Circuit . . . . .	39
4.3.1	Design And Test . . . . .	41
<b>5</b>	<b>rf-SQUID measurement</b>	<b>45</b>
5.1	Current-phase measurement . . . . .	45
5.2	NbN rf-SQUID current-phase characteristics . . . . .	46
5.3	Measurement . . . . .	47
5.4	Data analysis . . . . .	48
5.5	Experimental results . . . . .	49
<b>6</b>	<b>Conclusion</b>	<b>54</b>

# Chapter 1

## Introduction

It has been over a hundred years since the discovery of superconductivity by Kamerlingh Onnes. Superconducting materials exhibit quantum properties on a macroscopic scale that are already being utilized in healthcare, metrology, quantum cryptography, spintronics, and quantum computing [22] [12]. One of the most significant challenges is the development of quantum computers, which are based on utilizing the superposition of states to accelerate computation. However, it is crucial to maintain this superposition of quantum bit states for as long as possible. One of the main realizations of qubits are superconducting loops interrupted by a potential barrier, which are called SQUIDs. SQUIDs are very sensitive devices that react to magnetic fields. They are basically superconducting loops interrupted by a potential barrier, such as an insulator or normal metal Josephson junction. If the magnetic flux passing through them is half of the magnetic flux quantum  $\Phi_0/2$ , they enter a superposition of current flow directions, and the energy is the same for both current flow directions. However, this state is easily disrupted by surrounding noise. Therefore, researchers are exploring ways to prevent the disruption of this superposition. One of the predicted solutions is topologically protected insulators that are insulators in the bulk but have conductive states on the surface. Currently, the development of topological insulators is struggling with keeping the Majorana bound states, which cause the topological properties, unharmed. Thus, research is dedicated to searching for robust topological materials that maintain their properties.

This work is motivated by the development of an apparatus capable of measuring the properties of radiofrequency SQUIDs with the vision of measuring and analyzing topological Josephson junctions in the future. Therefore, it mainly focuses on the description of Josephson junctions and the Josephson effect, which are described in the chapter "Theory". We are also motivated by the development of SQUID production. We contribute to the development of production by analyzing a lithographically prepared nanobridge Josephson junction made of NbN, which we measured using the

apparatus designed by us and described in the chapter "Apparatus". We discuss the microscopic effects in SN interface junctions, namely Andreev reflections and Andreev bound states, and briefly show a possible way of measuring Majorana bound states in topological Josephson junctions. The analysis of the NbN Josephson junction can also contribute to the characterization of nanoscale NbN structures from which similar nanoscale meanders can be produced, which can capture a single photon. Therefore, we analyze the measured current-phase characteristic by applying theoretical models of clean and dirty short Josephson junctions described by Kulik and Omelyanchuk.

# Chapter 2

## Theory

In this chapter, we will explore the basic concepts of the microscopic theory of superconductivity, and subsequently focus on the mechanisms in Josephson junctions.

### 2.1 Superconductivity

In 1908, Heike Kamerlingh Onnes was the first person to successfully liquefy helium gas. This significant achievement opened up new possibilities for the development of cryogenic technologies, as it was now possible to achieve temperatures below 4.2 K using liquid helium as a refrigerant. This breakthrough started a new trend in condensed matter physics, as researchers began exploring the properties of various materials at extremely low temperatures.

Three years later, in 1911, Onnes discovered the phenomenon of superconductivity in several metals when they were cooled to low temperatures close to absolute zero. This discovery was a major milestone in the history of condensed matter physics, as superconductors are metals that, when cooled below a certain critical temperature ( $T_c$ ), exhibit zero resistance. At the time of this discovery, however, there was no explanation for this new phenomenon.

Further experimentation and measurement of superconductors showed that they act as ideal diamagnets in the presence of a magnetic field, completely expelling the field in what is known as the Meissner effect. The London brothers later developed a macroscopic theory to explain this effect, which postulated that a super-current arises in the superconductor when it is subjected to a magnetic field. This current flows to a depth of  $\lambda$ , which compensates perfectly for the field.

In the 1950s, Ginzburg and Landau studied the phase transition to the superconduct-

ing state as a second type of phase transition. They introduced an order parameter  $\Psi(\vec{r}) = \sqrt{n_S}e^{i\Theta(\vec{r})}$  as a pseudo wave function, where the amplitude represents the concentration of the superconducting charge. One of the results of their theory was that the supercurrent density is dependent on the phase gradient of the order parameter. However, despite these theories, the origin of superconductivity remained unexplained until Bardeen, Cooper, and Schrieffer (BCS) proposed a new theory in the 1950s. They explained superconductivity as a macroscopic coherent state of a Bose-Einstein condensate created by pairs of electrons, called Cooper pairs. They found that any positive interaction between two electrons under the critical temperature would decrease the energy of the system.

The microscopic explanation provided by BCS led to significant developments in observing superconducting microstructures and applications in technology. Researchers began studying various superconducting geometries, and Josephson predicted that it would be possible to observe a tunneling current of Cooper pairs through a potential barrier that interrupts two superconductors. This phenomenon was later named after Josephson, and it has become an important tool in quantum electronics, used for quantum bits, parametric amplifiers, and other applications..

## 2.2 Ginzburg-Landau order parameter and phase

Ginzburg and Landau proposed a different approach to understanding superconductivity several years after London's attempt. The Ginzburg-Landau (GL) theory explains superconductivity as a thermodynamic phase transition of the second type. It builds on Landau's theory of phase transitions, which suggests that any phase transition can be explained using an order parameter that ranges from 0 for a disordered system to 1 for an ordered system. This approach allowed for the description of second-type phase transitions, which was an unsolved problem during Landau's time.

In studying phase transitions, it is useful to consider the free energy. From thermodynamics, we know that the free energy  $F$  is minimized at equilibrium, and during the transition, the chemical potentials of the two phases are equal. Considering this equality of chemical potentials, which are also Gibbs free energies, we can derive the condensation energy of the superconducting state in an environment without gradients and fields to be  $U_C = f_s - f_n = -\frac{H_c^2}{8\pi}$ , where  $f_s$  and  $f_n$  are the free energy densities of the superconducting and normal states, respectively, and  $H_c$  is the critical magnetic field above which the superconducting state vanishes.

GL uses the pseudo-wave function  $\Psi(\vec{r}) = |\Psi(\vec{r})|e^{i\Theta(\vec{r})}$  as the order parameter of the superconducting state. The density of superconducting electrons is defined as the squared amplitude of this function,  $n_s = |\Psi(\vec{r})|^2$ . At temperatures close to the critical temperature  $T_C$ , where the material is superconducting, condensation energy  $U_C$  must be paid for the phase transition. Contributions to the superconducting free energy include  $F_s = F_n + U_C + KE + FE$ , where  $F_n$  denotes the normal state free energy,  $KE$  denotes kinetic energy and  $FE$  denotes magnetic field energy. Then the superconducting free energy is [8]

$$F_s = F_{n0} + \int d^3r \left( f_0 + \frac{1}{2m^*} \left| \left( \frac{\hbar}{i} \nabla - q_s \vec{A}(\vec{r}) \right) \Psi(\vec{r}) \right|^2 + \frac{H^2(\vec{r})}{8\pi} \right) \quad (2.1)$$

Where  $f_0 = f_s - f_n = -H_c^2/8\pi$  in the absence of fields and gradients and it can be viewed as Taylor expansion of free energy in powers of  $n_s$  [44] and it is also a condensation energy free density [33],[8]. The gradient term is accounting for a change of the wave function in the space, with a non-zero value of a vector potential  $\vec{A}$ , and the last term is the magnetic energy of a field penetrating the superconductor from outside.

The free energy is then integral over the space of the free energy density  $F = \int f \vec{r}^3$ . Following Ginzburg and Landau, we can consider  $F$  to be a functional of  $F[\Psi(\vec{r}), \Psi^*(\vec{r}), \vec{A}(\vec{r})]$ . Than the extremes of  $F$  in the  $\Psi(\vec{r})$  and  $\vec{A}(\vec{r})$  can be found by variational method taking  $\delta F = 0$ .

In general, the extreme of a functional can be found using the theorem of functional derivatives. The first GLE is derived from minimizing the functional F with respect to  $\Psi$ . Varying F as  $\Psi + \delta\Psi$  we get the 1.Ginzburg Landau equation:

$$\alpha(T)\Psi(\vec{r}) + \beta(T)|\Psi(\vec{r})|^2\Psi(\vec{r}) + \frac{1}{2m^*}(-i\hbar\vec{\nabla} - e^*\vec{A})^2 = 0 \quad (2.2)$$

And varying  $A + \delta A$  we get the 2. Ginzburg - Landau equation:

$$\vec{j}_S = \frac{c}{4\pi}\vec{\nabla} \times \vec{B} \quad (2.3)$$

$$= \frac{e^*\hbar}{2m^*i}(\Psi^*(\vec{r})\vec{\nabla}\Psi(\vec{r}) - \Psi(\vec{r})\vec{\nabla}\Psi^*(\vec{r}) - \frac{(e^*)^2}{m^*c}|\Psi|\vec{A}) \quad (2.4)$$

Inserting the order parameter function into the 2.GLE we get the equation :

$$\vec{j}_S = \frac{e^*|\Psi(\vec{r})|^2}{m^*}(\hbar\nabla\Theta - \frac{e^*}{c}A) \quad (2.5)$$

Taking few steps back to the free energy  $f_0 = \alpha(T)|\Psi(\vec{r})|^2 + \frac{1}{2}\beta(T)|\Psi(\vec{r})|^4$ , lets look closer to the GL parameters  $\alpha(T)$  and  $\beta(T)$ . For a minimum of  $f_0$  in  $|\Psi(\vec{r})|$  (We will write  $\Psi(\vec{r}) = \Psi$ ) we have to take the derivative and make it zero, thus

$$\frac{\partial}{\partial|\psi|}f_0 = 2\alpha(T)|\psi| + 2\beta(T)|\psi|^2 \quad (2.6)$$

$$|\psi|^2 = |\psi_\infty|^2 = -\frac{\alpha(T)}{\beta(T)} \quad (2.7)$$

Where  $|\psi_\infty|$  is the value of  $\Psi(\vec{r})$  of the free energy minimum, or the relaxed value. Since  $f_0 = -H_C^2/8\pi$ , inserting  $|\psi_\infty|$  in to the Eq.2.6 we see

$$\frac{\alpha(T)^2}{2\beta(T)} = \frac{H_C(T)^2}{8\pi} \quad (2.8)$$

### 2.2.1 Ginzbur-Landau Coherence Length

The simplest case of 1GLE is a one-dimensional line or wire, which can be used as a nanobridge approximation. For simplicity consider Eq.2.2 in one dimension for zero magnetic field  $\vec{A} = 0$

$$\alpha(T)\Psi + \beta(T)|\Psi|^2\Psi + \frac{\hbar^2}{2m^*}\nabla^2\Psi = 0 \quad (2.9)$$

Using substitution  $f(x) = \Psi/\Psi_\infty$ , where  $\Psi_\infty = -\alpha(T)/\beta(T)$  [44] the differential equation shrinks to

$$\frac{\hbar^2}{2m^*|\alpha(T)|}\frac{d^2f(x)}{dx^2} + f(x)^3 - f(x) = 0 \quad (2.10)$$

Where we define the characteristic length  $\xi(T)$  on which  $\Psi$  vary

$$\xi(T)^2 = \frac{\hbar^2}{2m^*|\alpha(T)|} \quad (2.11)$$

The quantity  $\xi$  is called a coherence length and it is a value on which the  $\Psi(x)$  slightly disturbed of  $\Psi_\infty$  decay [44]. The value of GL coherence length is

$$\xi = \frac{\Phi_0}{2\sqrt{2}\pi H_c(T)\lambda(T)} \quad (2.12)$$

where  $\Phi_0$  is magnetic flux quantum,  $H_c(T)$  is a critical magnetic field and  $\lambda(T)$  is penetration depth.

## 2.3 BCS

The first complete theory describing a microscopical origin of the superconductivity was developed by Bardeen - Cooper - Schrieffer for which they were awarded a Nobel Prize in 1972. A fundamental idea was to find out whether it is energetically convenient for pair of electrons to create a bound state since the electrostatic interaction between electrons should be positive. Cooper showed that the binding will appear for any positive attraction no matter how weak it is. In this section, we will show the basics of the BCS theory.

### 2.3.1 Cooper pairs

Consider a metal in the ground state at temperature  $T = 0$  K, so that all electrons have energies  $< E_F$ . Pair of electrons added above  $E_F$  can be described by a pair wave function, dependent on the position and momentum of each electron

$$\Psi(\vec{r}_1, \vec{r}_2, \vec{k}_1, \vec{k}_2) = e^{i(\vec{k}_1 \cdot \vec{r}_1 + \vec{k}_2 \cdot \vec{r}_2)} \quad (2.13)$$

Using the substitution of relative coordinates  $\vec{K} = \vec{k}_1 + \vec{k}_2$ ,  $\vec{k} = \frac{1}{2}(\vec{k}_1 - \vec{k}_2)$ ,  $\vec{r} = \vec{r}_1 - \vec{r}_2$  and  $\vec{R} = \frac{1}{2}(\vec{r}_1 + \vec{r}_2)$  we get new wave function as

$$\Psi(\vec{r}, \vec{R}, \vec{k}, \vec{K}) = e^{i(\vec{K} \cdot \vec{r} + \vec{k} \cdot \vec{R})} \quad (2.14)$$

When the system is statical and there is no current flow, the system is in the lowest energy state. Thus the total momentum  $\vec{K} = \vec{k}_1 + \vec{k}_2 = 0$  and  $\vec{k}_1 = -\vec{k}_2 = \vec{k}$ , which means that our system depends only on the relative coordinates. Here is important to mention that for pair of electrons, it is most probable to create a singlet pair, since the relative coordinate  $\vec{r}$  is spherically symmetrical. In this case such electron pair state will have momentum  $(\vec{k}_\uparrow, -\vec{k}_\downarrow)$  where arrows are symbolizing spin up  $\uparrow$  and spin down  $\downarrow$ .

In that regard interactions between electrons can be expressed as a probability of electron pair occupying the state with energy of magnitude  $|\hbar\vec{k}|$ . The total wave function will be the sum of all possible states weighted by their probability

$$\Phi(\vec{r}) = \sum_{\vec{k}} g(\vec{k}) e^{i\vec{K} \cdot \vec{r}} \quad (2.15)$$

where  $g(\vec{k})$  is the weighting factor and it denotes the amplitude of the probability of occupying the particular state. We assume the  $g(\vec{k}) = 0$  for momentum below Fermi energy level  $k < k_F$  and  $g(\vec{k}) > 0$  to be close to the Fermi energy level since all states under the Fermi sea are occupied at the ground state.

Using the time independent Schrodinger equation  $(2\epsilon_k + V_{kk'})\Phi = E\Phi$  the interaction can be derived from  $(E - 2\epsilon_k)g(\vec{k}) = \sum_{k'>k_F} V_{kk'}g(\vec{k}')$  as [44]

$$V_{kk'} = \frac{1}{\Omega} \int d\vec{r} V(\vec{r}) e^{i(\vec{k}' - \vec{k}) \cdot \vec{r}} \quad (2.16)$$

where  $V_{kk'}$  characterizes the strength of the potential to scatter a pair of electrons with momentum  $(\vec{k}, -\vec{k})$  to the state  $(\vec{k}', -\vec{k}')$ , where  $\Omega$  is a normalization volume. The potential has values  $V_{kk'} = -V_0$  for energies below cut-off energy  $\epsilon_C = \hbar\omega_C$  and  $V_{kk'} = 0$  for all energies above the  $\epsilon_C$ . Applying it to the Schrodinger equation we obtain

$$(E - 2\epsilon_k)g(\vec{k}) = \sum_{k'>k_F} V_{kk'}g(\vec{k}') \quad (2.17)$$

$$= -V_0 \sum_{k'>k_F} g(\vec{k}') \quad (2.18)$$

$$(2\epsilon_k - E)g(\vec{k}) = V_0 \sum g(\vec{k}') \quad (2.19)$$

$$\frac{1}{V_0} = \frac{1}{\sum_{k>k_F} (2\epsilon_k - E)}. \quad (2.20)$$

Converting the summation to the integration we find

$$\frac{1}{V_0} = \int_{k_F}^{\epsilon_C} \frac{k'^2}{2\pi^2} \frac{1}{2\epsilon_k - E} dk' \quad (2.21)$$

$$= N(0) \int_{E_F}^{E_F + \epsilon_C} \frac{1}{2\epsilon - E} d\epsilon \quad (2.22)$$

$$= \frac{1}{2} N(0) \ln \left( \frac{2E_F - E + 2\hbar\omega_C}{2E_F - E} \right) \quad (2.23)$$

where we have used density of states on Fermi energy  $N(0) = \frac{k'^2}{2\pi^2} \frac{dk'}{d\epsilon}$  assuming the cut energy to be  $\epsilon_C \ll E_F$ . In most superconductors, it is found that  $N(0)V_0$  is  $< 0.3$  [44], so we can use weak coupling approximation  $N(0)V_0 \ll 1$ , in which the reduced eigenvalue energy of a pair  $U = E - E_F$  has value [33]

$$U \approx -2\hbar\omega_C e^{-2/N(0)V_0} \quad (2.24)$$

The outcome tells us that with any small amount of positive interaction  $V_0$ , the energy  $U$  will be reduced, thus it is advantageous to create an electron pair bound state. In other words, the Fermi Sea is unstable against the formation of a Cooper pair if there is any attractive interaction.

It has been proven that an electron attraction is caused by electron-phonon interaction.

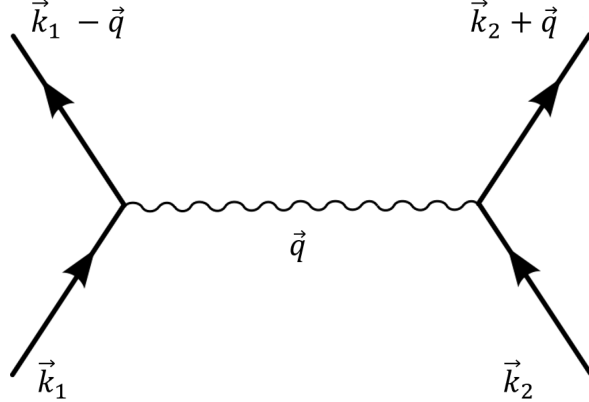


Figure 2.1: Feynman diagram of Cooper pair bounding: The process of binding two electrodes to the CP can be depicted by Feynman diagram. Electron with momentum  $\vec{k}_1$  emits a phonon  $\vec{q}$ , while second electron  $\vec{k}_2$  accepts the phonon  $\vec{q}$  resulting with momentum  $\vec{k}_2 + \vec{q}$ . The total momentum is conserved  $\vec{K} = \vec{k}_1 - \vec{q} + \vec{k}_2 + \vec{q} = \vec{k}_1 + \vec{k}_2$

[7] The main idea is that an electron passing through the crystal lattice with momentum  $\vec{k}$  creates a small charge density deviation hence vibrating the lattice and creating a phonon with momentum  $\vec{q}$ . This phonon is absorbed by a second electron with momentum  $-\vec{k}$  lowering the energy of the system and creating a Cooper pair, while the total momentum of pair is generally conserved  $\vec{K} = \vec{k}_1 + \vec{k}_2 = (\vec{k}_1 - \vec{q}) + (\vec{k}_2 + \vec{q})$ . The existence of CP is then determined with the upper limit of phonon eigenvalue frequencies, which are bounded by Debye energy, thus the critical energy limit should be  $\epsilon_C \approx \hbar\omega_D$ , where  $\omega_D = k_B\Theta_D/\hbar$  is Debye frequency and  $\Theta_D$  is Debye temperature.

### 2.3.2 The BCS ground state

We have shown that the ground state of a metal at zero temperature will change because of the positive interaction between electrons. It is natural to look for a new ground state with Cooper pairs states. We know that for two electrons in state  $(\vec{k}_\uparrow, -\vec{k}_\downarrow)$  scattering into a state  $(\vec{k}'_\uparrow, -\vec{k}'_\downarrow)$ , the state has to be free before accepting a phonon, and after creating the pair the previous state has to be unoccupied. We can think about that in the way, that there has to be a non-zero probability to unoccupied states  $(\vec{k}'_\uparrow, -\vec{k}'_\downarrow)$  so electrons can scatter. With the probabilistic formulation, the reduced Hamiltonian for the ground state will be [33]

$$U = 2 \sum_{\vec{k}} \epsilon_{\vec{k}} v_{\vec{k}}^2 - 2 \sum_{\vec{k}, k < k_F} \epsilon_{\vec{k}} + \sum_{\vec{k}, \vec{k}'} V_{\vec{k}\vec{k}'} u_{\vec{k}} v_{\vec{k}} u_{\vec{k}'} v_{\vec{k}'} \quad (2.25)$$

where  $v_{\vec{k}}^2$  denotes probability of occupation of state  $(\vec{k}_\uparrow, -\vec{k}_\downarrow)$  and  $v_{\vec{k}}^2 + u_{\vec{k}}^2 = 1$  has to be fulfilled. The first two terms of Hamiltonian are the difference in kinetic energy

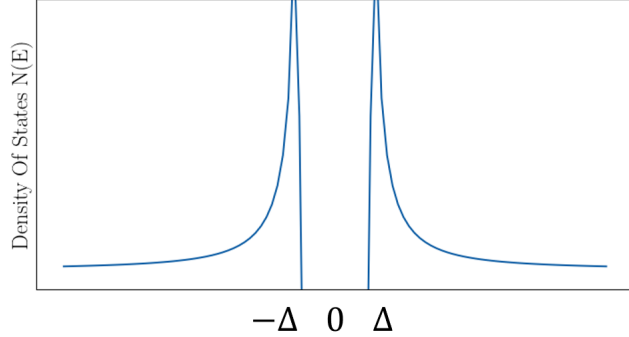


Figure 2.2: Density of states of the ground state  $T = 0$ . All states under energy  $-\Delta$  are occupied and all above  $\Delta$  are free. If we consider positive temperature  $T > 0$  quasiparticles will excite to states above  $\Delta$ . In the interval  $(-\Delta, \Delta)$  there will be only Cooper pairs.

of a CP and ordinary electrons.

Hence minimising the energy  $U$  in respect of probability  $v_{\vec{k}}^2$  we get the value of probability  $v_{\vec{k}}^2$  for equilibrium state

$$v_{\vec{k}}^2 = \frac{1}{2} \left( 1 - \frac{\epsilon_{\vec{k}}}{E_{\vec{k}}} \right) \quad (2.26)$$

where quantity  $E_{\vec{k}} = \sqrt{\epsilon_{\vec{k}}^2 + \Delta_{\vec{k}}^2}$  is the excitation energy of quasi-particles and  $\Delta_{\vec{k}} = -\sum_{\vec{k}'} V_{\vec{k}\vec{k}'} u_{\vec{k}'} v_{\vec{k}'}$  is the energy gap. The excitation energy has an important meaning. It is the total energy difference between one quasi-particle state and a bound state energy of probability  $v_{\vec{k}}^2$  with value

$$E_k = \epsilon_k (1 - 2v_{\vec{k}}^2) + 2u_k v_k \Delta_k. \quad (2.27)$$

The fact that the probability  $v_{\vec{k}}^2 > 0$  at  $T = 0K$  around the Fermi energy is stunning. If we depict the relation between probability and energies, we would see that in the superconducting state, the probability is smeared around Fermi energy  $E_F$  on the interval  $(E_F - \Delta_{\vec{k}}, E_F + \Delta_{\vec{k}})$ , compared to the metal ground state which has sharp boundary at  $E_F$ .

The condensation energy  $E_C$  as a difference between the energy of the superconducting state and the normal state can be computed, giving a relation

$$E_C = -N(0) \frac{\Delta^2}{2}. \quad (2.28)$$

To destroy a CP, one-electron states with opposite momentum have to be unoccupied, then the Cooper pair decays to quasi-particle states. Quasi-particles are particles that

come from Cooper pair decay, especially electrons called - quasi-electrons (qe) and holes - quasi-holes (qh). For temperatures higher than absolute zero  $T > 0$ , we expect thermally excited quasi-particles to appear and thus we would have to account for a Fermi-Dirac distribution to the Hamiltonian. The result would be leaking quasi-particle states close to the  $\Delta$  value.

### 2.3.3 Energy gap

The energy gap is one of the main attributes of superconductors. In the BCS approach, we assume the value for  $\Delta_{\vec{k}}$  to have values  $\Delta$  for kinetic energies below Debye energy  $< \hbar\omega_D$  and 0 for higher energies. In the zero temperature limit  $T = 0$ , the energy necessary to break a CP is exactly a  $2\Delta$ . At the finite temperature, the relation for the energy gap reads

$$\Delta_k = - \sum_{k'} V_{kk'} u_{k'} v_{k'} (1 - 2f(E_{k'})) \quad (2.29)$$

where  $f(E_{k'})$  is Fermi dirac distribution of quasi-particles. Using BCS approximation the interaction potential is

$$\frac{1}{V} = \frac{1}{2} \sum_{\vec{k}} \frac{\tanh\left(\frac{E_{\vec{k}}}{2k_B T}\right)}{E_{\vec{k}}}. \quad (2.30)$$

Similarly we get relation of  $\frac{1}{N(0)V_0}$  in the integral form, which has solution  $k_B T_C \approx 1.13\hbar\omega_C$  for the weak coupling approximation  $N(0)V_0 \ll 1$ . Substituting to the Eq.2.29 [44]

$$\Delta(0) \approx 1.764k_B T_C. \quad (2.31)$$

For the nonzero temperatures  $T > 0$ , the energy gap shrinks. A good approximation for its temperature dependence close to critical temperature is [41] [33]

$$\Delta(T) \approx 1.74\Delta(0)\sqrt{1 - T/T_C}. \quad (2.32)$$

In the energetic spectrum of quasi-particles, there is a forbidden interval of width  $2\Delta$  in which no quasi-particle can exist, which leads to the dependence of the density of quasi-particle states on the energy gap. Density follows a  $\Delta(T)$  dependence, hence with rising temperature, there is a positive number of states above the cut energy because the fermion particle's excitation energy must be a positive quantity.

### 2.3.4 Coherence length

Coherence length  $\xi$  is one of the important values which characterizes superconductors. Throughout the history of superconductivity, it has had different definitions. The microscopical BCS definition is that it is the mean size of a Cooper pair, or in other words mean length on which the bound electron pair arises. In the Ginzburg-Landau(GL) theory it is a length on which the order parameter recovers. This can appear at the superconductor-normal metal interface where the superconducting state disappears [ref Roy]. The BCS coherence length  $\xi_0$  is also a low temperature limit of GL coherence length  $\xi_{GL}$ , thus  $\xi_{GL}(T \rightarrow 0) = \xi_0$  [34]. The  $\xi_0$  for pure superconductor reads

$$\xi_0 = \frac{\hbar v_F}{\pi \Delta} \quad (2.33)$$

where  $v_F$  is Fermi velocity,  $\Delta$  is the energy gap.

## 2.4 Josephson effect

Cooper pairs in superconductor make up a coherent state on the length  $\xi$ , since two bounded fermions create a boson, at some temperature  $T_{BE}$  they align in the phase-coherent state thus creating a Bose-Einstein condensate. Usually the temperature  $T_{BE}$  is lower than the critical temperature of superconductivity  $T_C$ . In the phase-coherent state the Bose-Einstein condensate acts as one particle, therefore we describe the whole system by one macroscopic wave function. Josephson predicted that in a superconductor interrupted with a potential barrier, Cooper pairs would tunnel through it resulting in a superconducting current with sinusoidal dependence on wave function phase difference  $\varphi$ . Later has been shown [24] that the Josephson effect is valid generally for Bose-Einstein condensates, which is also a superfluid state of He. In two chambers connected by a weak link, e.g. capillary, filled with superfluid helium, the superfluid is creating a periodical movement and the oscillations can be heard as a whistle [40]. In this section, we derive and show the Josephson effect in the quantum approach of a tunnel junction and we will show the effects of cooper pair transport in weak link junctions.

### 2.4.1 Josephson junctions

Josephson junction(JJ) is generally a weak link between two superconducting electrodes by which the junctions can be classified. We differ JJ's to tunnel junctions in which the superconducting current flow by tunneling through the potential barrier and to the weak links with direct current flow mediated by proximity effect. Tunnel junctions are usually superconductor-isolator-superconductor SIS sandwiches. They can be manufactured by letting a metal oxidize a few microns thin insulating layer, e.g. Al - Al<sub>2</sub>O<sub>3</sub> - Al sandwiches. There are various types of weak links. A weak link can be made of the normal-conductivity region called an SNS junction, from a superconductor with lower critical current noted as SS'S junctions or by altering the geometry of a superconductor. Narrowing the superconductor to a nano-bridge structure cause higher current density in the constriction which after exceeding the critical current density value destroys superconductivity. Thus these weak links are called constriction junctions ScS. [30] [23]

JJs have a large spectrum of applications. Most commonly are used SIS junctions because of the simplicity of their manufacture and mainly due to low dissipation. From Josephson junctions are made parametric amplifiers, quantum bits, magnetometers,

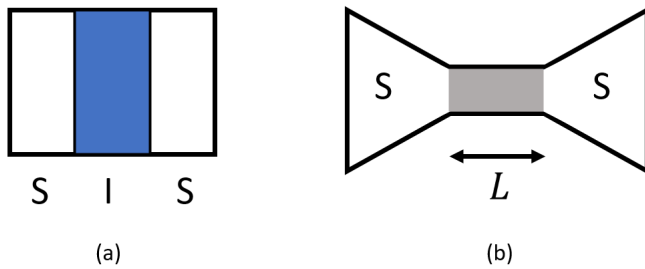


Figure 2.3: Main types of Weak links. (a) Tunnel Josephson junction, (b) Constriction Josephson junction. The gray constriction could be made from normal metal or superconductor with different critical current values. If the junction has constant thickness it is called Dayem bridge.

voltage standard devices, or also microwave lasers. [23]

## Weak Links Classification

For any weak link, the length of the junction  $L$ (Fig.2.3.). The effective length  $L_{eff}$  is the distance at which a non-linear effect starts to appear. Non-linear effects cause variations in the order parameter which lead to a change in the value  $|\Delta|$  of electrodes. Appropriate classification of weak links is to compare effective length  $L_{eff}$  with the characteristic lengths of material from which the weak link is made: the mean free path  $l$ , and the coherence length  $\xi$ .

JJ's with  $L_{eff} \ll \xi$  are classified as short while  $L_{eff} \geq \xi$  as long junctions. It turns out that the ideal Josephson effect shows up in the short junctions, while the rise of  $L_{eff}$  causes considerable deviations.

However even for short junctions the Josephson effect will not be ideal depending on the mean free path  $l$ . The junctions which have  $L_{eff} \gg l$  are called "dirty" and for the opposite limit "clean" junctions. Here it is important to point out that by dirty we don't mean the notion of "dirty limit" which is used in BCS theory. [30]

### 2.4.2 Quantum Josephson effect of tunnel junction

For simplicity, we start to describe the effects of tunnel Josephson junction. To show the quantum Josephson effect we will use Heisenberg [15] approach, which is appropriate for short tunnel junctions. In the beginning, it is necessary to introduce basic quantum-mechanical relations. We will be working in phase representation, in which the phase operator  $\hat{\phi}$  and number of particles  $\hat{n}$  obey postulated commutation rule analogically to the position and momentum operators  $\hat{x}, \hat{p}$  [24] [21] [31] [24]

$$[\hat{n}_j, \hat{\varphi}_j] = i \quad (2.34)$$

from which the operators can be written as derivatives [24]

$$\hat{\varphi}_j = i \frac{\partial}{\partial \hat{n}_j}, \quad (2.35)$$

$$\hat{n}_j = -i \frac{\partial}{\partial \hat{\varphi}_j}. \quad (2.36)$$

It is convenient to introduce annihilation and creation operators as Dirac decomposition

$$\hat{a}_j = \sqrt{\hat{n}_j + 1} e^{i\hat{\varphi}_j} \quad (2.37)$$

$$\hat{a}_j^\dagger = e^{-i\hat{\varphi}_j} \sqrt{\hat{n}_j + 1} \quad (2.38)$$

where  $i = \sqrt{-1}$  is imaginary number. Hence the annihilation and creation operators obey the common commutation rule

$$[\hat{a}_i, \hat{a}_j^\dagger] = \sqrt{\hat{n}_i + 1} e^{i\hat{\varphi}_i} e^{-i\hat{\varphi}_j} \sqrt{\hat{n}_j + 1} - e^{-i\hat{\varphi}_j} \sqrt{\hat{n}_j + 1} \sqrt{\hat{n}_i + 1} e^{i\hat{\varphi}_i} \quad (2.39)$$

$$= \sqrt{\hat{n}_i + 1} e^{i\hat{\varphi}_i} \sqrt{\hat{n}_j} e^{-i\hat{\varphi}_j} - \sqrt{\hat{n}_j} e^{-i\hat{\varphi}_j} \sqrt{\hat{n}_i + 1} e^{i\hat{\varphi}_i} \quad (2.40)$$

$$(2.41)$$

for  $i = j$ :

$$\begin{aligned} [\hat{a}_i, \hat{a}_j^\dagger] &= \sqrt{\hat{n}_i + 1} \sqrt{\hat{n}_i + 1} e^{-i\hat{\varphi}_i + i\hat{\varphi}_i} - \sqrt{\hat{n}_j} \sqrt{\hat{n}_i + 1} e^{i\hat{\varphi}_i - i\hat{\varphi}_i} \\ &= \hat{n}_i + 1 - \hat{n}_i = 1 \end{aligned}$$

for  $i \neq j$ :

$$[\hat{a}_i, \hat{a}_j^\dagger] = 0. \quad (2.42)$$

Therefore the commutator is the Kronecker delta,

$$[\hat{a}_i, \hat{a}_j^\dagger] = \delta_{ij}. \quad (2.43)$$

The annihilation and creation operators satisfy relations

$$\hat{a}|n\rangle = \sqrt{n}|n-1\rangle \quad (2.44)$$

$$\hat{a}^\dagger|n\rangle = \sqrt{n+1}|n\rangle \quad (2.45)$$

where  $|n\rangle$  is eigenstate of  $\hat{n}$ .

The operators  $\hat{a}, \hat{a}^\dagger$  can be also understood as a definition for the phase operator, which was proposed by Dirac [35]. However, the expression  $e^{i\hat{\varphi}}$  is not a unitary operator at the boundaries of the Fock basis, thus the rigorous definition of the phase operator  $\hat{\varphi}$  has to be taken carefully. Another definition of  $\hat{\varphi}$  which gives (2.38) reads

$$e^{i\hat{\varphi}_j} = \sum |\hat{n}_j\rangle\langle\hat{n}_j + 1| \quad (2.46)$$

$$e^{-i\hat{\varphi}_j} = \sum |\hat{n}_j + 1\rangle\langle\hat{n}_j|. \quad (2.47)$$

From this, we can see that (2.46) decreases state by one particle and (2.47) increase state by one particle. Operator  $\hat{n}$  and the phase operator  $\hat{\varphi}$  than satisfy commutation rule

$$[\hat{n}_j, e^{\pm i\hat{\varphi}_j}] = \hat{n}_j e^{\pm i\hat{\varphi}_j} - e_j^{\pm i\hat{\varphi}} \hat{n}_j \quad (2.48)$$

$$= \hat{n}_j e^{\pm i\hat{\varphi}_j} - (\hat{n}_j \pm 1) e^{\pm i\hat{\varphi}_j} \quad (2.49)$$

$$= \mp e^{\pm i\hat{\varphi}_j}. \quad (2.50)$$

The process of tunneling can be described as taking away one Cooper pair from the left superconductor and adding it to the right superconductor. The delocalization of the Cooper pair decreases the energy of the Josephson junction by the tunneling energy  $\mathcal{T}$  which can be expressed by the tunneling Hamiltonian

$$\mathcal{H}_J = -\mathcal{T} (\hat{a}_1^\dagger \hat{a}_2 + \hat{a}_1 \hat{a}_2^\dagger). \quad (2.51)$$

It is convenient to rewrite the tunneling Hamiltonian by making use of new operators: a number of bosons imbalance operator  $\hat{n} = (\hat{n}_1 - \hat{n}_2)/2$ , the total number of particles  $N = \hat{n}_1 + \hat{n}_2$ , and the phase difference operator  $\hat{\varphi} = \hat{\varphi}_2 - \hat{\varphi}_1$ ,

$$\begin{aligned} \mathcal{H}_J &= \mathcal{T} \left( e^{-i\hat{\varphi}_1} \sqrt{\hat{n}_1 + 1} \sqrt{\hat{n}_2 + 1} e^{i\hat{\varphi}_2} + \sqrt{\hat{n}_1 + 1} e^{i\hat{\varphi}_1} e^{-i\hat{\varphi}_2} \sqrt{\hat{n}_2 + 1} \right) \\ &= \mathcal{T} \left( \sqrt{\hat{n} + N/2} \sqrt{N/2 - \hat{n} + 1} e^{i\hat{\varphi}} + \sqrt{N/2 + \hat{n} + 1} \sqrt{N/2 - \hat{n}} e^{-i\hat{\varphi}} \right) \\ &= \mathcal{T} \left[ \left( \sqrt{\hat{n} + N/2} \sqrt{N/2 - \hat{n} + 1} + \sqrt{N/2 + \hat{n} + 1} \sqrt{N/2 - \hat{n}} \right) \cos \hat{\varphi} + \right. \\ &\quad \left. + \left( \sqrt{\hat{n} + N/2} \sqrt{N/2 - \hat{n} + 1} - \sqrt{N/2 + \hat{n} + 1} \sqrt{N/2 - \hat{n}} \right) i \sin \hat{\varphi} \right]. \end{aligned}$$

Since the tunneling of Cooper pair charge the Josephson junction with capacitance  $C$  by charging energy  $E_C = (2e)^2/2C$ , the total Hamiltonian reads

$$\mathcal{H} = E_C(\hat{n} - n_0)^2 - \mathcal{T} (\hat{a}_1^\dagger \hat{a}_2 + \hat{a}_1 \hat{a}_2^\dagger), \quad (2.52)$$

the time evolution of the system is given by Heisenberg equations

$$\dot{\hat{n}} = \frac{1}{i\hbar} [\hat{n}, \mathcal{H}] \quad (2.53)$$

$$= -\frac{1}{\hbar} \left( \frac{\partial}{\partial \hat{\varphi}} \mathcal{H} + \mathcal{H} \frac{\partial}{\partial \hat{\varphi}} \right) \quad (2.54)$$

$$= i \frac{\mathcal{T}}{\hbar} \left( \sqrt{\hat{n} + N/2} \sqrt{N/2 - \hat{n} + 1} e^{i\hat{\varphi}} - \sqrt{N/2 + \hat{n} + 1} \sqrt{N/2 - \hat{n}} e^{-i\hat{\varphi}} \right), \quad (2.55)$$

$$\dot{\hat{\varphi}} = \frac{1}{i\hbar} [\hat{\varphi}, \mathcal{H}] \quad (2.56)$$

$$= \frac{2E_C}{\hbar} (\hat{n} - n_0) + \frac{2\mathcal{T}}{\hbar} \left( \frac{2\hat{n} - 1}{\sqrt{\hat{n} + N/2} \sqrt{N/2 - \hat{n} + 1}} + \frac{2\hat{n} + 1}{\sqrt{N/2 + \hat{n} + 1} \sqrt{N/2 - \hat{n}}} \right). \quad (2.57)$$

If  $\langle \hat{n} \rangle \gg 1$  the tunneling Hamiltonian can be reduced to

$$\mathcal{H}_J \simeq -N\mathcal{T} \sqrt{1 - \left( \frac{2\hat{n}}{N} \right)^2} \cos \hat{\varphi}, \quad (2.58)$$

where  $N\mathcal{T} = E_J$  is Josephson energy. Hence, the Cooper pairs current  $\dot{\hat{n}}$  can be expressed as

$$\dot{\hat{n}} \simeq -\frac{E_J}{\hbar} \sqrt{1 - \left( \frac{2\hat{n}}{N} \right)^2} \sin \hat{\varphi}, \quad (2.59)$$

similarly, the phase evolution reads

$$\dot{\hat{\varphi}} = \frac{2E_C}{\hbar} (\hat{n} - n_0) + \frac{4E_J}{\hbar} \frac{\hat{n}}{\left( \frac{2\hat{n}}{N} \right)^2} \cos \hat{\varphi}. \quad (2.60)$$

In the limit of small particle imbalance,  $\langle \hat{n} \rangle \ll N$ , the (2.59) is the well-known first Josephson equation

$$I_S = I_C \sin \varphi,$$

and the (2.60) is the second Josephson equation

$$\dot{\hat{\varphi}} = -2n_0 \mathcal{U}/\hbar,$$

where  $I_C = E_J/\hbar$  is the critical current. The above equations are valid for macroscopic tunnel junctions as well as for weak links close to the critical temperature  $T_C$ . [44] [30]

## 2.5 Normal Metal And Constriction Junctions

### 2.5.1 Andreev reflection

Josephson junctions are a typical example of an inhomogeneous system in the superconductor-normal conducting region contact. [23] The electrons flowing from

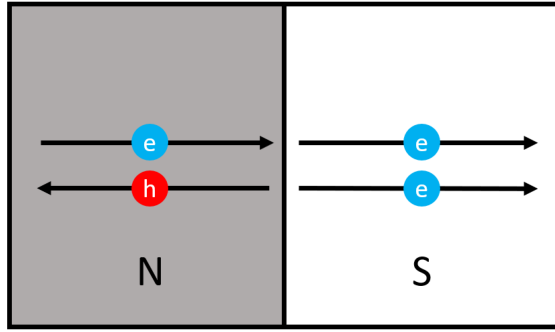


Figure 2.4: Andreev reflection: In the NS interface, the superconductivity leaks in the form of Andreev reflection. It can be imagined as electrons with energy in the energy gap could pass from the N region to the superconductor only if they take a second electron to a pair, reflecting a hole.

the normal conductor to the superconductor cannot pass if they have energy below the energy gap in the superconductor. Classically, the electrons in the normal metal should be reflected from the superconductor. However, the electron can be reflected from the metal/superconductor interface as a hole. This effect was investigated by A.F. Andreev in 1964 and was named after him as Andreev's reflection. Such phenomenon can be microscopically described by the Bogoliubov - de Gennes Hamiltonian

$$\mathcal{H}_{BdG}(\vec{r}) = \begin{pmatrix} H_0(\vec{r}) & -\Delta(\vec{r}) \\ -\Delta^*(\vec{r}) & -H_0(\vec{r}) \end{pmatrix},$$

$$H_0(\vec{r}) = -\frac{\hbar^2}{2m} \nabla^2 - \mu + V(\vec{r}).$$

The exact theoretical derivation of Andreev's reflection is given in [43].

The results of the Bogoliubov-de Gennes theory can be interpreted as follows. Electron with energy  $E$  traveling from a normal state passing in the superconductor recombines with a quasi-electron with opposite energy  $-E$  and opposite momentum and spin from the normal conductor, therefore creating a Cooper pair in the superconductor (Fig.2.4).

Hence the incident electron is leaving behind the hole traveling in the opposite direction to the electron's original way, such that the charge and momentum are conserved. The hole wave function additionally picks up a phase  $\varphi$  depending on the energy of the incident electron and also the phase of the superconducting wave function. The problem with the missing charge caused by the retro-reflected hole can be explained only by adding it to the superconducting condensate. This stands on the fact that the quasi-particle states cannot accommodate the charge, since they are evanescent. The Cooper pairs leak into the normal metal in the form of electron-hole pairs inducing

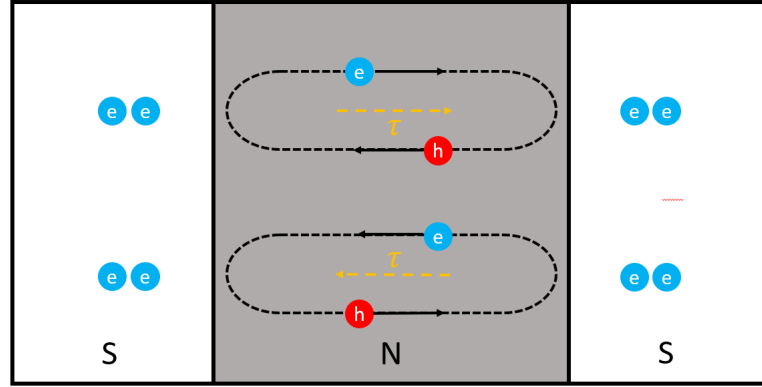


Figure 2.5: Andreev Bound States: The ABS from only if the phase across the junction is mod $2\pi$ . Each pair has its partner with opposite energy.

superconductivity. This phenomenon is called the superconducting proximity effect.

### 2.5.2 Andreev bound states

In the weak link, Josephson junctions can be considered as the normal conductor region with two interfaces with the superconducting electrodes where the Andreev reflections occur. At zero applied voltage the Cooper pair from the left superconductor decay to a counter-propagating quasi-particle electron-hole pair as shown in Fig.2.5. Electron and hole acquire a phase due to Andreev reflection as well as by traveling through the weak link. The total phase difference gained across the junction with length L reads

$$\varphi_{tot} = \varphi_{h \rightarrow e}(E, \varphi_1) + \varphi_L + \varphi_{e \rightarrow h}(E, \varphi_2). \quad (2.61)$$

The first term refers to the phase acquired on the left SN interface. It is dependent on the phase of the left superconductor wave function  $\varphi_1$ .

Similarly, the last term is the phase gained from the right NS interface and finally, the middle term is the phase accumulated while traversing the normal region. The picked-up phase on the interfaces is dependent on the coupling electron energy  $E$ . The phases  $\varphi_1$  and  $\varphi_2$  can be obtained by comparing the S-wave function with the N-wave function. Since the coherent state has to be maintained through the weak link, a total phase has to have values

$$\varphi_{tot} = \pm 2\pi n, \quad n = 0, 1, 2, \dots \quad (2.62)$$

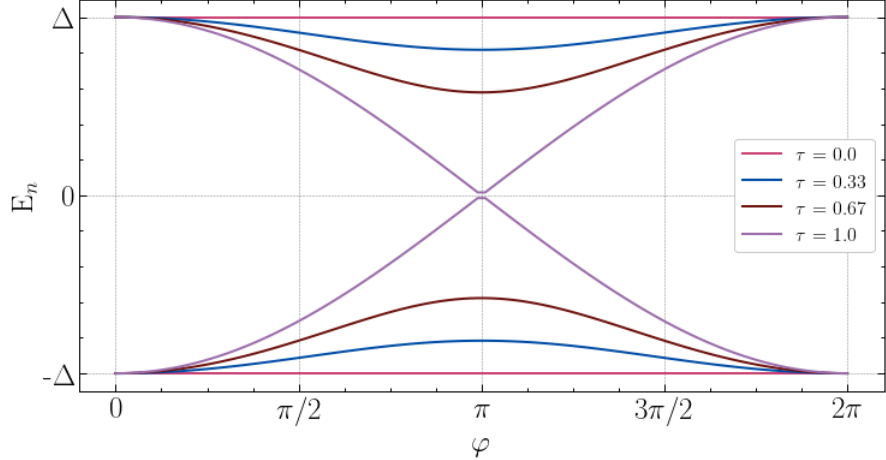


Figure 2.6: Energy  $E_n$  - phase  $\varphi$  dependence. Changing the value of  $\tau_n$  from 0 to 1 the energy value at  $\varphi = \pi$  is approaching zero. For the value  $\tau = 1$ , the gap between the ground and 1st excitation state is smallest, however,s it never crosses.

Hence the superconducting current flows only in discrete total phase values which implicate the existence of quasi electron-hole bound states with discrete energy levels below the energy gap value, which are called Andreev bound states (ABS). Due to the symmetry reasons every bound state has its partner with an opposite transfer channel, thus with opposite energies  $E^+ = -E^-$ . If the Andreev reflection dominates, the Cooper pairs are emitted for each reflection on the right side, and reversely on the left interface are absorbed. Therefore, the superconducting current flows through the junction. [23]

The energy excitations of Andreev levels will depend on the total phase value [28], which depends on the junction architecture and material. A step change usually models SNS junctions in the pair potential  $\Delta(x)$

$$\Delta(x) = \begin{cases} \Delta e^{i\varphi_1}, & x < 0 \\ 0, & 0 < x < L \\ \Delta e^{i\varphi_2}, & x > L \end{cases}$$

where  $\Delta$  is the energy gap and  $x$  is the position in the junction of length  $L$ . Considering the normal region to be short we may neglect the term  $\varphi_L$ .

In short weak links,t  $L_{eff} \ll \xi$ , the Andreev energy levels depend on the phase difference across the junction  $\varphi = \varphi_2 - \varphi_1$  and the transparency of the nth transfer channel  $\tau_n$

$$E_n^\pm = \pm \Delta \sqrt{1 - \tau_n \sin^2(\varphi/2)}, \quad (2.63)$$

where the  $\pm$  sign symbolizes a particular component of the bound pair considering its direction, plus sign is for electrons moving right, and the minus sign is for electrons moving left.

### 2.5.3 Current-Phase Relationship

To find the maximum value of the Josephson current that ABS can carry, we can examine generated bound state power [23]

$$P = \frac{\partial}{\partial t} E_n^\pm = \frac{\partial E_n^\pm}{\partial \varphi} \frac{2eV}{\hbar} = I_n^\pm V. \quad (2.64)$$

Here we use the second Josephson equation in order to express the time derivative of the phase  $\varphi$  and define the current of the nth transition channel

$$I_n^\pm = \frac{2e}{\hbar} \frac{\partial E_n^\pm}{\partial \varphi}. \quad (2.65)$$

The ABS is composed of fermion particles, electrons, and holes in normal metal, and therefore at the equilibrium state the population of energy states with energies  $E^+$  and  $E^-$  are given by Fermi-Dirac distribution function

$$f(E_n^\pm) = \frac{1}{e^{\frac{E_n^\pm}{k_B T}} + 1}. \quad (2.66)$$

Thus, the total superconducting current flowing through the junction will be the sum of contributions of all populated energy states

$$I_S(\varphi) = \frac{2e}{\hbar} \left( \sum_n \frac{\partial E_n^-}{\partial \varphi} f(E_n^-) + \sum_n \frac{\partial E_n^+}{\partial \varphi} f(E_n^+) \right). \quad (2.67)$$

Since  $E_n^- = -E_n^+$  and  $I_n^- = -I_n^+$  the current-phase relationship can be written in the final form

$$I_S(\varphi) = \frac{e\Delta}{2\hbar} \sin(\varphi) \sum_n \frac{\tau_n}{\sqrt{1 - \tau_n \sin^2(\varphi/2)}} \tanh \left( \Delta \frac{\sqrt{1 - \tau_n \sin^2(\varphi/2)}}{2k_B T} \right). \quad (2.68)$$

In the tunneling limit  $\tau_n \rightarrow 0$  the Ambegaokar- Baratoff relation is reproduced [23] [30]

$$I_S(\varphi) = \frac{\pi\Delta}{2eR_N} \tanh \left( \frac{\Delta}{2k_B T} \right) \sin(\varphi). \quad (2.69)$$

### 2.5.4 Short Junctions In Dirty Limit

Until now, we have considered short Josephson junctions  $L \ll \xi$  in the clean limit  $\xi \ll l$ . In highly disordered superconductors,  $\xi \gg l$  the current-phase relationship can be found for arbitrary junction geometries. If the temperature is close to the critical temperature  $T_C$  the G-L theory can be used. The GL equations in dirty limit read [30]

$$\begin{aligned} \xi^2 \left( \vec{\nabla} - i \frac{2e}{\hbar c} \vec{A} \right)^2 \Delta + \left[ \pm 1 - \frac{|\Delta|^2}{\Delta_0^2} \right] \Delta &= 0, \\ \vec{j}_S &= C_j \mathcal{I} \left[ \Delta^* \left( \vec{\nabla} - i \frac{2e}{\hbar c} \vec{A} \right) \Delta \right], \end{aligned}$$

where

$$\xi^2(T) = \frac{\pi\hbar D}{9k_B(T_C - T)} \quad (2.70)$$

is coherence length,  $D = v_F l/3$  is diffusion coefficient,  $v_F$  is Fermi velocity,  $\Delta_0$  is the characteristic value of order parameter amplitude  $|\Delta|$  which for temperatures close to  $T_C$  is equivalent to equilibrium value and parameter  $C_j = \pi\sigma_N/ek_B T$  is proportional to the normal conductivity  $\sigma_N$  in the dirty limit. Usadel introduced a solution for these GL equations with a complex function that only depends on point  $F(\vec{r})$  and on Matsubara frequency

$$\hbar\omega = \pi k_B T(2n + 1), \quad n = 0, 1, 2, \dots \quad (2.71)$$

where the Usadel's superconducting current density is

$$\vec{j}_S = \frac{2\pi\sigma_N k_B T}{e} \sum_{\omega>0} \mathcal{I} \left[ F^* \left( \vec{\nabla} - i \frac{2e}{\hbar c} \vec{A} \right) F \right]. \quad (2.72)$$

Using Eq. (2.72) Kulik - Omelyanchuk derived the current-phase relationship for short dirty junction

$$I_S = \frac{2\pi k_B T}{eR_N} \sum_{\omega>0} \frac{2\Delta \cos(\varphi/2)}{\delta} \arctan \left( \frac{\Delta \sin(\varphi/2)}{\delta} \right), \quad (2.73)$$

where  $\delta = \sqrt{\Delta^2 \cos^2(\varphi/2) + (\hbar\omega)^2}$ . [30]

### 2.5.5 Dayem nanobridges

Dayem bridges are nanobridges that have a constant thickness but the width of the nanobridge is patterned to a constriction. In contrast to other types of nanobridges, Dayem bridges exhibit weak current concentration, meaning that the current is not confined to specific channels but is spread out. It is difficult to determine their effective length  $L_{eff}$ , which is defined by the points between which the phase should be taken. Likharev and Yakobson analyzed [30] the case of nanobridges where the bridge length is close to or larger than the coherence length of the thin film. Let's consider a 1D micro-bridge with the condition  $\xi \ll L$ , and we also assume reduced magnetic fields  $\vec{A} = 0$ . Introducing a wave function in the form  $f(x) = a(x)e^{i\varphi(x)}$  the Ginzburg-Landau equation can be written in the form

$$\xi \frac{da(x)}{dx} = \sqrt{a_0^2 - \frac{a_0^4}{2} + \frac{j_0^2}{a_0^2} - a^2(x) + \frac{a(x)^4}{2} - \frac{j_0^2}{a(x)^2}}. \quad (2.74)$$

For the boundary conditions of the wave function amplitude,  $a(0) = a(L) = 1$  must hold, so that the function  $f(x)$  is equal to the superconducting wave functions  $\Psi_\infty$  at

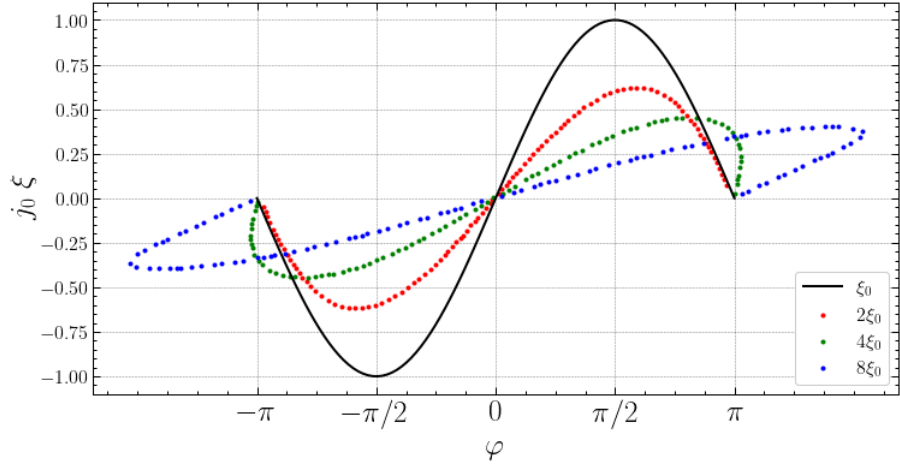


Figure 2.7: Dayem bridge: Scaled current density  $j_0\xi$  - phase  $\varphi$  dependence. The sinusoidal current-phase dependence tilts for different values of the coherence length. The used dataset was borrowed from [39].

the edges of the bridge. Using GL equations, it can be shown [39] that the length of the bridge satisfies

$$L = 2\xi \int_{a_0}^1 \frac{da}{\sqrt{a_0^2 - a(x)^2 + \frac{a(x)^4 - a_0^4}{2} + j_0^2 \left( \frac{1}{a_0^2} - \frac{1}{a(x)^2} \right)}}, \quad (2.75)$$

where  $a_0 = a(L/2)$ . Thus, the phase difference  $\varphi$  can be expressed in the form

$$\varphi = 2j_0\xi \int_{a_0}^1 \frac{da}{\sqrt{a_0^2 - a(x)^2 + \frac{a(x)^4 - a_0^4}{2} + j_0^2 \left( \frac{1}{a_0^2} - \frac{1}{a(x)^2} \right)}}. \quad (2.76)$$

Such a problem can be numerically solved by finding two solutions for  $j_0$  and  $a_0$ . The current-phase relationship becomes nonsinusoidal for long bridges, while the short bridges satisfy standard  $\sin(\varphi)$  dependence.

# Chapter 3

## Current-phase relationship

To measure the current-phase relationship of the Josephson current one can use a superconducting quantum interference device (SQUID). These devices are superconducting loops that contain at least one Josephson junction. SQUID with only one junction is called "radio-frequency" -rf SQUID, which can be measured by inductively coupled tank circuits. A loop with two junctions is called "direct current"-dc SQUID and it can be measured directly by applying dc current. In this chapter, we will discuss the fundamental properties of rf-SQUIDs.

### 3.1 Magnetic Flux In The Superconducting Loop

In the Ginzburg-Landau theory section in Chapter 2, we have shown that a superconductor can be described by the order parameter  $\psi(\vec{r}) = |\psi(\vec{r})|e^{i\Theta(\vec{r})}$ . Considering a continuous superconducting ring, the phase  $\Theta$  of the order parameter around the ring must be modulo  $2\pi$  to ensure that the order parameter is single-valued and that the physical properties of the superconductor remain unchanged. If the ring is thick enough, the superconducting current flows within a depth of  $\lambda$ , and we can find a path for which the current density  $\vec{j} = 0$ . In the presence of a non-zero magnetic field passing through the superconducting ring, the following relation holds

$$\nabla\Theta = \frac{q}{\hbar}\vec{A}, \quad (3.1)$$

where  $q = 2e$  is the charge of a Cooper pair. The magnetic flux through the ring is given by:

$$\Phi = \int \vec{B} \cdot d\vec{S}, \quad (3.2)$$

By applying Stokes theorem and substituting the value for  $\vec{A}$ , we obtain the equation for the magnetic flux:

$$\Phi = \oint \nabla \Theta(\vec{r}) \cdot d\vec{r}, \quad (3.3)$$

Due to the phase condition, the following relation must hold:

$$\Phi = 2\pi n \frac{\hbar}{2e} \quad n = 0, 1, 2, \dots \quad (3.4)$$

This implies that the magnetic flux is quantized, specifically in multiples of the magnetic flux quantum with an experimentally determined value of  $\Phi_0 = h/2e$  (approximately  $2.07 \times 10^{-15}$  Wb), where  $h$  is the Planck constant. [33] [44]

## 3.2 Magnetic Flux In The rf-SQUID

Adding Josephson junction into the superconducting loop (Fig. 3.1) violates condition  $j_s = 0$  in the loop. This condition is satisfied inside the body of the superconductor but not inside the Josephson junction. If we apply a magnetic field at the rf-SQUID the total magnetic flux is the sum of the external magnetic flux  $\Phi_e$  and the superconducting response  $\Phi_S$ . Since the superconducting current in the Josephson junction has some current-phase relationship  $I_S(\varphi)$  the total flux will be

$$\Phi = \Phi_e - LI_S(\varphi) \quad (3.5)$$

$$= \Phi_e - LI_C \sin \varphi, \quad (3.6)$$

where  $L$  is the loop inductance and  $I_S = I_C \sin \varphi$  is the Josephson current. If the superconductor is wider than the penetration depth  $\lambda$ , the superconducting current density is zero inside,

$$\vec{j}_s = \frac{\hbar}{m} \left( \nabla \Theta - \frac{2e}{\hbar} \vec{A} \right) = 0, \quad (3.7)$$

inside the superconductor

$$\nabla \Theta = \frac{2e}{\hbar} \vec{A}. \quad (3.8)$$

Let us assume that there is a gauge invariant phase difference  $\varphi$  across the junction

$$\varphi \equiv \int_1^2 (\nabla \Theta - \frac{2\pi}{\Phi_0} \vec{A}) \cdot d\vec{s}, \quad (3.9)$$

where  $\Phi_0 = h/2e$  is the magnetic flux quantum. Using Eqs. 3.7 and  $\Phi = \oint \vec{A} \cdot d\vec{s}$  one can see that the phase difference across the junction depends on magnetic flux

$$\varphi = \oint \nabla \Theta d\vec{s} - \frac{2\pi}{\Phi_0} \Phi = 2\pi n - 2\pi \Phi / \Phi_0. \quad (3.10)$$

Thus one can write transcendental equation for  $\varphi$  substituting (3.6)

$$\varphi = 2\pi n - \varphi_e + \frac{2\pi L}{\Phi_0} I_S(\varphi), \quad (3.11)$$

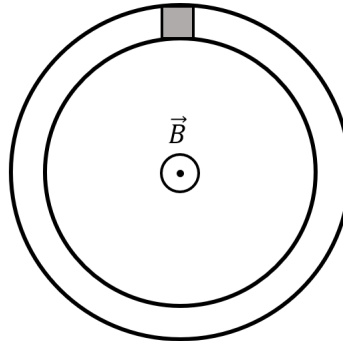


Figure 3.1: rf-SQUID in a magnetic field. The Josephson junction is symbolized by the grey region.

where  $\varphi_e = 2\pi\Phi_e/\Phi_0$  is the normalized external magnetic flux. [4] [44] This equation doesn't have a closed solution since the screening field depends on the  $I(\varphi)$  and vice versa.

### 3.2.1 Screening Effect

The non-linear phase dependence on the external magnetic flux is called a screening effect. As can be seen from (3.11) the rf-SQUID has two working regimes which are defined by its response: hysteretic and non-hysteretic. The current-phase relationship can be calculated numerically or shown graphically. For simplicity, we will show graphically the sinusoidal Josephson current. Let's consider the rf-SQUID in the constant external field with biasing resonance circuit  $\Phi_e = \Phi_{dc} + \Phi_{rf}$  creating a periodical magnetic flux through the loop. In the hysteretic regime when  $2\pi L I_C / \Phi_0 > 1$  the screening effect will be a sinusoidal behavior superimposed on a linear one, thus some regions will have positive and some negative tilts. This is caused by the large contribution of the Josephson current to the total magnetic flux in the rf-SQUID.

In the limit  $2\pi L I_C / \Phi_0 \ll 1$  the magnetic flux  $\Phi \approx \Phi_e$  and the screening effect have nearly linear dependence. If the rf-SQUID is coupled to the tank circuit,  $\varphi \approx \varphi_e$ , and the Josephson current can be measured by changing the external magnetic flux with the tank circuit. [23] [4]

## 3.3 Majorana bound states detection

Coupling the resonant circuit to the rf-SQUID can be used to measure the Majorana bound states(MBS). MBS are predicted to appear in topological Josephson junctions

[42] or in semiconducting nanowires, [27]. MBS similarly to Andreev bound states depends on the phase difference  $\varphi$  across the junction and the junction transparency  $\tau$ . However, they have different dependencies of equidistant energy levels

$$E^\pm = \pm\sqrt{\tau}\Delta \cos(\varphi/2). \quad (3.12)$$

Thanks to the different parity of MBS, in comparison to the same parity of Andreev bound states, the energy values can cross each other at the point  $\varphi = \pi$ , which can be imagined as a quasi-particle exchange between energy levels. This results in a  $4\pi$  periodicity of the Josephson current across the junction [45], or of the energy. Such excitation can be relaxed back to the ground state depending on some perturbations. Thus the lifetime of a Majorana excitation is severely influenced by the dynamical coupling to the quasi-particle environment. Any high enough perturbation might relax the Majorana state. Hence to observe the  $4\pi$  periodicity it will be necessary to use out-of-equilibrium rf measurements at frequencies fast enough so the excited state won't relax and thus restore the  $2\pi$  periodicity of Josephson junction. [23]

# Chapter 4

## Apparatus

The main problem of measuring quantum phenomena is thermal noise and also all surrounding fields which can interfere with the measured signal. There are several common methods used to suppress such interference. For example, the external fields can be suppressed by electromagnetic shielding. The superconducting shields are very efficient in the suppression of low-frequency magnetic fields. Shields are also needed in the process of cooling.

To measure the current-phase characteristics we have designed and created a measuring apparatus that consists of RC- mixer filters, a tank circuit, and a low-noise amplifier. The apparatus was designed to fit into the refrigerator which will be described in this chapter. A low-noise amplifier is connected to the 3K refrigerator plate. Wires tend to create loops through the circuitry, which catch magnetic fields and induct parasitical currents. A simple solution for this problem is to create a twisted pair, which cancels the inducted currents. This method will be used to connect the amplifier with a tank circuit anchored to the 300 mK refrigerator plate. The wires are made from superconducting alloy which also suppresses thermal conductivity. High-quality coaxial cables are used to connect the amplifier with room-temperature electronics. In this section, we describe the design and construction of the measuring apparatus.

## 4.1 Refrigerator

The difficulty to approach temperatures close to 0 K increase exponentially, however today it isn't a big deal to achieve a temperature as 3 Kelvins. All our measurements were carried out at low temperatures  $T = 0.3 \text{ K}$  to  $3 \text{ K}$ . We have used a dry  $^3\text{He}$  Oxford Heliox AC-V refrigerator which uses a pulse tube for cooling.

### 4.1.1 Pulse Tube

To accomplish low temperatures, different concepts of dry cryocoolers were historically used as Joule-Thompson expansion, Stirling cycles, or pulse tubes. All of them let the working gas perform against internal or external forces. By dry refrigerators, we mean closed-cycle refrigerators, conceptually similar to common food refrigerators, where refrigerants are circulating and periodically reused. Another way to refrigerate is by dipping samples right into the refrigerant having direct thermal contact with working gas. As a refrigerant one would use helium gas  $^4\text{He}$  to reach temperatures below 10 K since its suitable properties are at low temperatures and relatively available price.  $^4\text{He}$  liquefies at  $T = 4.2 \text{ K}$  at pressure 1 bar and turns into the superfluid state at lambda point temperature  $\approx 2.1 \text{ K}$ . The biggest disadvantage of helium is its small value of latent heat  $l = 21 \text{ kJ/kg}$ . Compared to the nitrogen with  $k = 200 \text{ kJ/kg}$ . This is the main reason why is not very economical to use helium in wet refrigerators. Using mechanical pistons in the Stirling cycle finds its limit at temperatures  $T < 50 \text{ K}$ , since oils and lubes enable the piston to move freeze. The solution to this problem is a Pulse tube, which uses helium as a virtual piston made of compressed working gas, hence allowing it to reach even lower temperatures.

The principle is based on a pressure wave generator which is periodically pushing the working gas. The heat created by compressing is absorbed by the heat exchanger connected to the regenerator commonly made of porous magnetic material with high heat capacity. The regenerator also serves separator between the compressor and the pulse tube. Helium flowing to the volume reservoir through an orifice expands hence lowering its temperature on the heat exchanger(heat end of the tube). Gas flowing back from the reservoir through the pulse tube to the compressor absorbs heat from the regenerator providing the cooling power. Part of helium never escapes the tube space, thus compressed volume acts like a piston. This is achieved by precisely adjusting the velocity of the working gas and the frequency of the pressure wave generator.

Two pulse tube coolers stages can provide temperatures around 2 K with  $^4\text{He}$  gas at pressures  $\approx 15 \text{ bar}$  since the cooling power is dependent on the working gas thermal

expansion coefficient which goes to zero at that temperature. [38] [6].

### 4.1.2 $^3\text{He}$ pot

To achieve even lower temperatures than  $^4\text{He}$  the  $^3\text{He}$  isotope is commonly used. This can be done thanks to the  $^3\text{He}$  higher vapor pressures at the same temperatures compared to the  $^4\text{He}$ . The advantage coming from  $^3\text{He}$  usage is the heat capacity rate of change, which is way larger for  $^4\text{He}$ . Also, the heat capacity of  $^3\text{He}$  in the liquid state is larger than for liquid  $^4\text{He}$  below 1.4 K. The last significant property is the superfluid transition temperature,  $^3\text{He}$  isn't superfluid at temperatures  $T > 0.3$  K. Superfluid  $^4\text{He}$  can escape through very thin space. Since the superfluids have highly efficient thermal conductivity coming from zero viscosity, leaking out of the chamber can cause thermal shorts in the refrigerator. The critical condensation temperature of  $^3\text{He}$  is  $T = 3.3$  K. After reaching this temperature the  $^3\text{He}$  condensates and hence can be captured in the pot. To cool down liquefied  $^3\text{He}$  in dry cryo-coolers zeolites or porous adsorbents as carbon, with large surfaces are used. These so-called sorption pumps can be controlled by heat switches, for example from a heating coil and superconducting wire thermally connected to the pulse tube stage with a lower temperature. Heating the sorption pump helium evaporates by increasing pressure, and by cooling the pump down using a heat-switch, which switches the thermal connection by superconducting wire, enabling the sorption pump to adsorb the gas by lowering the bath temperature. [38]

### 4.1.3 Refrigerator Assembly

Oxford Heliox apparatus uses two pulse tube stages to achieve  $T = 3$  K and carbon sorption pump adsorbing  $^3\text{He}$  vapors from the  $^3\text{He}$  pot, thus having 4 temperature stages shown in figure Fig.4.1. The cooling process starts with attaching aluminum shields to the refrigerator plates thus thermally connecting them to the temperature stages. Shields are necessary to suppress heat radiation from surrounding, since helium's latent heat is very low, with poor radiation shielding the cooling possibilities will be limited.

When the refrigerator is closed the membrane vacuum pump is used for pre-vacuum. Under good conditions, we expect to reach 5.5 mbar after 40 minutes. After that we use a turbo-molecular vacuum pump until the pressure is around  $8.6 \times 10^{-6}$  mbar, thus reaching ultra-high vacuum, which takes around 12 hours. The compressor pumps  $^4\text{He}$  gas into the first stage of pulse tube PTC1 thermally connected to the 40 K plate, and to the second tube PTC2 cooling the 3K plate, which is thermally connected to the  $^3\text{He}$  tubes heading to 0.3 K plate. By cooling down the 3K plate also  $^3\text{He}$  cools down, hence the pressure in the  $^3\text{He}$  chamber decreases with its thermal conductivity. With

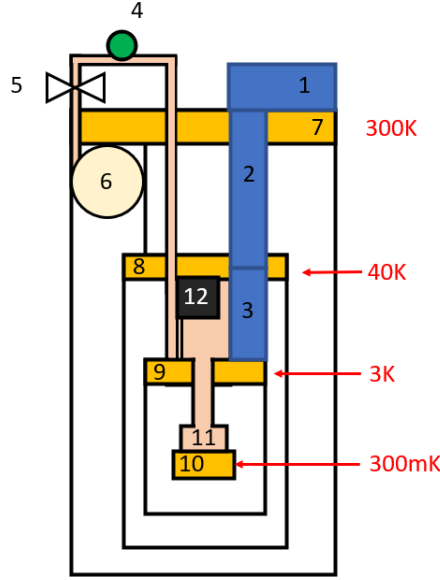


Figure 4.1: Refrigerator construction: 1. Pulse tube rotor, 2. Pulse tube first cycle PTC1, 3. Second pulse tube cycle PTC2, 4. barometer, 5. orifice, 6.  ${}^3\text{He}$  chamber, 7. 300 K plate with shield, 8. 40 K plate with equipped shield, 9. 3K plate with shield, 10. 300 mK plate, 11.  ${}^3\text{He}$  pot, 12. sorption pump.

a heat switch connected to the carbon sorption pump, we can control the pressure of  ${}^3\text{He}$  cycle. Heating the sorption pump  ${}^3\text{He}$  evaporates and condensates at the cold surface of the  ${}^3\text{He}$  pot trickling to the bottom. Cooling down the sorption pump by heat-switch, the porous material is ready to adsorb helium vapors. This is done several times until the temperature cools down to  $\approx 3.5$  K. than setting the heat-switch to  $T = 25$  K we can achieve temperature  $\approx 330$  mK in about 25 minutes. [20] [38]

## 4.2 Amplifier

The superconducting currents flowing through Josephson junctions are extremely low, usually in the range  $10^{-9} - 10^6$  A. For such low signal measurements, one has to suppress noises in the apparatus. This is partially done by cooling the measurement space by refrigerator since thermal noise power depends linearly on the temperature. Therefore, the signal should be amplified at low temperature by cryogenic amplifier to a level, which is much higher than the noise at room temperature.

### 4.2.1 Thermal Noise

Generally, noise can be defined as "any kind of disturbance that obscures or interferes with a desired signal" [13]. Thermal noise, which is one of the fundamental noises, is intrinsic, thus it can't be removed but can be suppressed by cooling. Thermal

noise cannot be exactly predicted, since it is the stochastic random motion of electrons, however, the randomness is predictable since much noise has a Gaussian distribution of instantaneous amplitudes with time [13]. Electrons flowing with trough wires, active and passive electronic parts are being slowed down by the environment's non-zero resistance. Classically we define resistance in macroscopic scale by Ohm's law  $V = RI$ . Microscopically it can be explained by interactions between free electrons and lattice vibrations - phonons of the conductor. At non-zero temperatures free electrons randomly vibrate, moving in a Brownian-like motion, this locally creates random charge density deviations or local currents. Thus average current is zero. Electron fluctuations are dependent on the resistance of the ion environment or in other words on electron-phonon interactions. The ion environment is incapable to compensate for the charge deviation creating a potential difference, hence we see the so-called noise voltage[32]. Thus the noise voltage depends on the temperature as

$$v = \sqrt{4k_B T R \Delta f}, \quad (4.1)$$

where  $k_B$  = is Boltzmann constant,  $R$  is resistance, and  $\Delta f$  is bandwidth defined as frequency interval for 50 % power drop from maximum power value or -3 dB in the logarithmic scale. The temperature dependence directly shows a way to decrease thermal noise. For example comparison of cooled apparatus with  $\Delta f = 1$  Hz,  $R = 1\text{k }\Omega$  and temperature 3 K with the same settings on 300 K temperature the noise ratio will be  $v_{3K}^2/v_{300K}^2 = 1/100$ .

#### 4.2.2 Amplifier Noise

Amplifiers are composed also of resistive components which create thermal noise in the amplifier. The thermal noise of an amplifier can be modeled as a noise-free black box and all internal sources can be represented by a voltage noise generator and a current noise generator usually at the input to the amplifier [13]. In Fig. is the amplifier noise model circuit scheme which adds noise-generating resistance  $R_S$  and a voltage source  $V_S$  as input to the amplifier. Here is convenient to define a system gain as the ratio of the signal source and amplifier output signal  $V_S/V_o$ , which varies with frequency. To sum noise we have to sum its squared values, then the noise output will be gained noise input  $E_i$  with factor A

$$E_{no}^2 = A^2 E_i^2. \quad (4.2)$$

The value of  $E_i^2$  can be also expressed as

$$E_i^2 = (E_t^2 + E_n^2) \left| \frac{Z_i}{Z_i + R_S} \right|^2 + I_n^2 \left| \frac{Z_i}{Z_i + R_S} \right|^2, \quad (4.3)$$

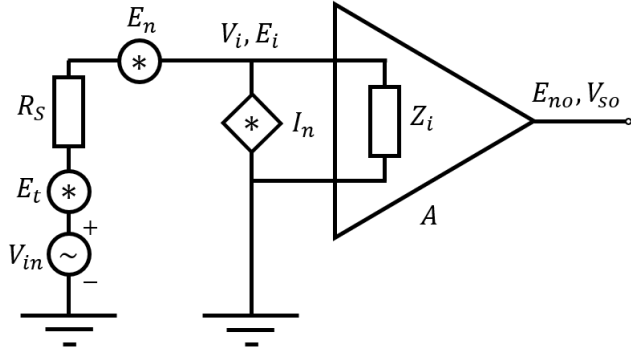


Figure 4.2: Amplifier noise model.

where  $E_t^2$  is the thermal noise generator of additive resistance  $R_S$ ,  $E_n$ ,  $I_n$  are noise voltage and current generators of an amplifier and  $Z_i$  is amplifier input impedance. It follows from this that the total input noise to the noise-less amplifier can be interpreted as the ratio of noise output and system gain, which gives us a relation

$$E_{ni}^2 = E_t^2 + E_n^2 + I_n^2 R_S^2. \quad (4.4)$$

While  $E_{in}$  is single input noise that will produce the same output noise as  $E_{no}^2$ . Thus for the zero  $R_S$  the first and third terms will drop out and the amplifier noise could be measured from output easily since then  $E_{no}^2 = A^2 E_n^2$ .

Let's imagine two amplifiers in a series. Both of them generate noise. If we define a noise factor  $F$  at room temperature  $T = 300$  K as

$$F = \frac{S_i/N_i}{S_o/N_o}, \quad (4.5)$$

where  $S_i/N_i$  is the input signal-to-noise ratio and  $S_o/N_o$  is for output ratio. Using the definition the noise factor for the first amplifier in the chain can be written as

$$F_1 = \frac{N_o}{G_o k_B T \Delta f}, \quad (4.6)$$

where  $N_o$  is the output noise power and  $G_o$  is the available power gain. The expression  $k_B T \Delta f$  is thermal noise power input since it equals  $E_t^2/4R_S$ . The input noise to the second amplifier can be expressed as  $N_{o2i} = F_1 G_1 k_B T \Delta f$ . Similarly, the noise factor of the second amplifier is

$$F_2 = \frac{N_{o2}}{G_{o2} k_B T \Delta f}, \quad (4.7)$$

and we can calculate the noise added in the second stage

$$(F_2 - 1) G_2 k_B T \Delta f. \quad (4.8)$$

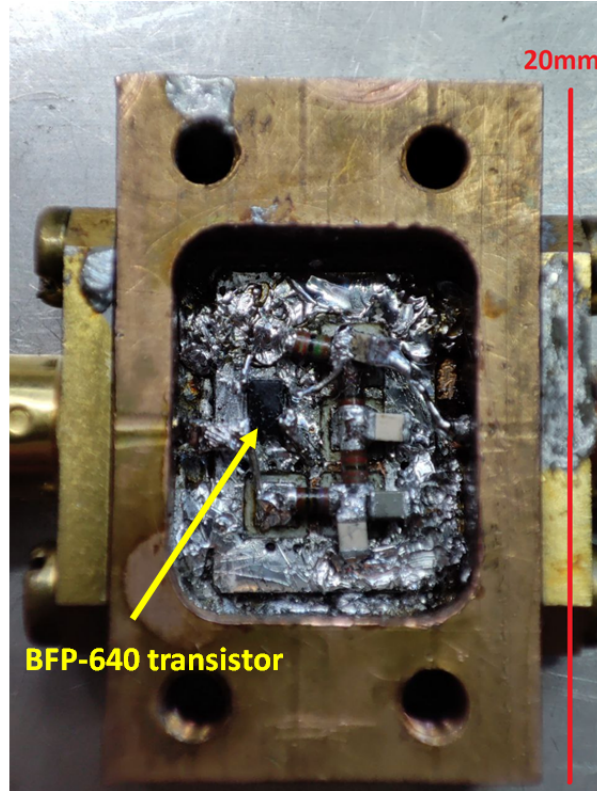


Figure 4.3: Construction of the cryogenic amplifier.

The noise factor of the whole system can be derived from Eq.4.6, Eq.4.7 and Eq.4.8

$$F_{12} = \frac{(F_1 G_1 G_2 + F_2 G_2 - G_2) k_B T \Delta f}{G_1 G_2 k_B T \Delta f} \quad (4.9)$$

$$= F_1 + \frac{F_2 - 1}{G_1}. \quad (4.10)$$

We can see that the noise of the second amplifier won't play an important role in the chain if the gain of the first amplifier is high. [13]

#### 4.2.3 Amplifier Design, Construction, and Test

The first design of a low-temperature amplifier was presented in my bachelor thesis [11]. It was designed to work at temperature  $T = 3$  K, using low noise bipolar transistor BFP-360 Si-Ge. The electronic architecture is shown in the picture Fig.4.4. Components were soldered to PCB 6 mm wide and 10 mm long Fig.4.3.

The device was then inserted and conductively connected with solder to a copper box, which was later joined to L - a shaped copper holder thermally anchored to a 3K refrigerator plate applying high vacuum Apiezon grease on the contact surface. The circuit was simulated in the program LT-SPICE [1]. We have simulated amplification and output noise dependence on the temperature using the circuit scheme in Fig.4.3.

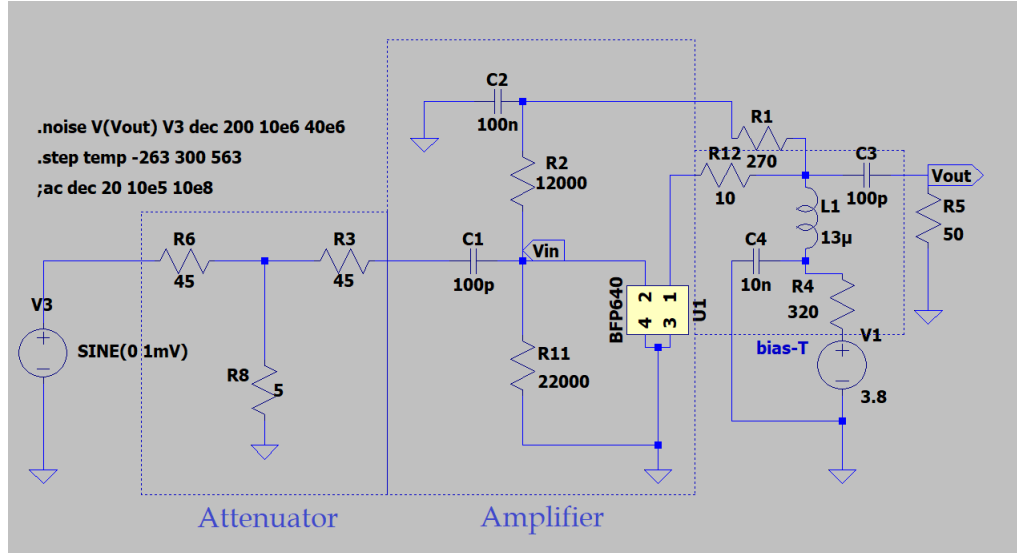


Figure 4.4: Simulated electric circuit of the apparatus in the LT-SPICE.

### Amplification Measurement

To measure amplifier transmission the Vector Network Analyser (VNA) had been used, using working voltage amplitude  $V = 3.8$  V and applied VNA power 0 dBm. Amplification measurements had been carried out on the room temperature  $T_r = 300$  K and low temperature  $T_l = 10$  K. The measurements set-up is shown in Fig.4.7.

To prevent VNA damage three attenuators with attenuation of -20 dB had been used. Before the amplification measurement, the commercial minicircuit amplifier amplification was measured. From the minicircuit datasheet [2] we found out the typical value of magnification of one amplifier was +22 dB for frequency intervals up to 100 MHz. For the measurement 3 minicircuit amplifier had been used, which corresponds to amplification +66 dB, while the exact value has been measured using VNA at room temperature(Fig.4.8). The cable attenuation was also measured at room temperature, with measured characteristics shown in Fig.4.9.

### Output And Input Noise Measurements

The amplifier output noise measurement was carried out with Power Spectral Analyser (PSA). Connecting a -20 dB attenuator with resistance  $50 \Omega$  to the amplifier, we can measure the amplified noise coming from the amplifier (Fig.4.11). Attenuator and amplifier noises are amplified and then suppressed by cables and the second time amplified by a commercial amplifier on the temperature  $T_r$ . In the logarithmic scale, we

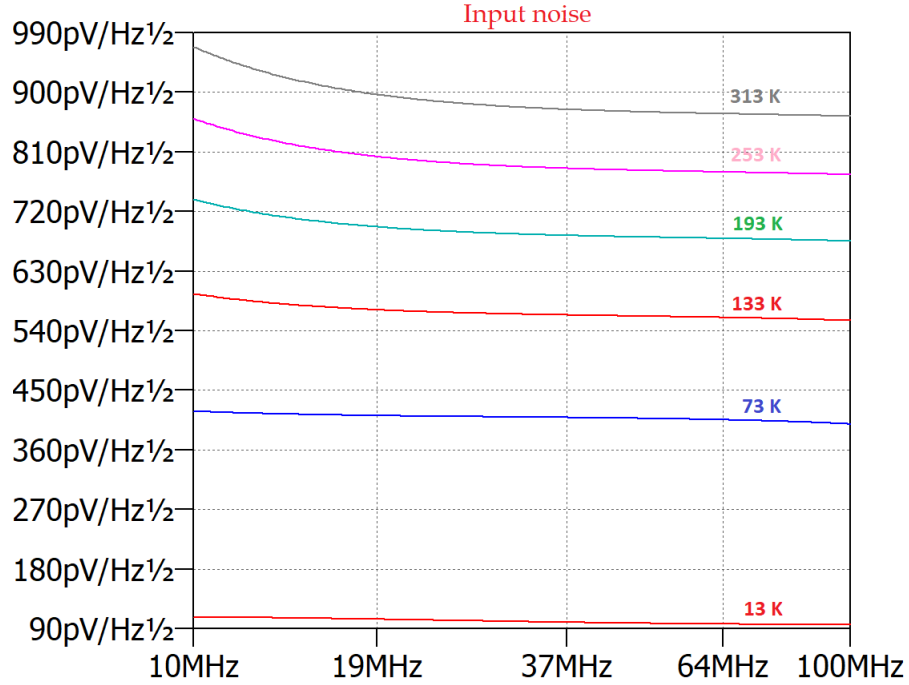


Figure 4.5: Input noise characteristics simulated in LT-Spice at various temperatures.

can describe the PSA input signal as

$$S = S_{out} + A - K + MC. \quad (4.11)$$

Since the measured data were displayed on the PSA in volts, converting to the linear scale the output signal relation is

$$S_{out} = \frac{10^{S/20}}{10^{(N_{calibrated}+K+AT)/20}}, \quad (4.12)$$

where  $N_{calibrated} = MC + A - 2K - AT$  is calibration. In this particular case, we have included also the amplification A. Thus the amplifier input noise will obey

$$v \left( \frac{V}{\sqrt{Hz}} \right) = \frac{S_{out}}{\sqrt{\Delta f}}, \quad (4.13)$$

where  $\Delta f = 1$  MHz is the bandwidth of the PSA.

The input noise was measured for the On and Off amplifier at temperatures  $T_r$  and  $T_l$ , while the PSA settings were  $\Delta f = 1$  MHz and video bandwidth = 510 Hz.

## Results

The simulation estimated the amplifier amplification to be +22 dB and the amplification rises with temperature decrease (Fig.4.10). Measurement proved qualitatively the simulation results (Fig.??, Fig.4.6). Simulating the amplifier input noise the simulation (Fig.4.5) predicted values in the order of magnitude  $nV/\sqrt{Hz}$ , thus for room

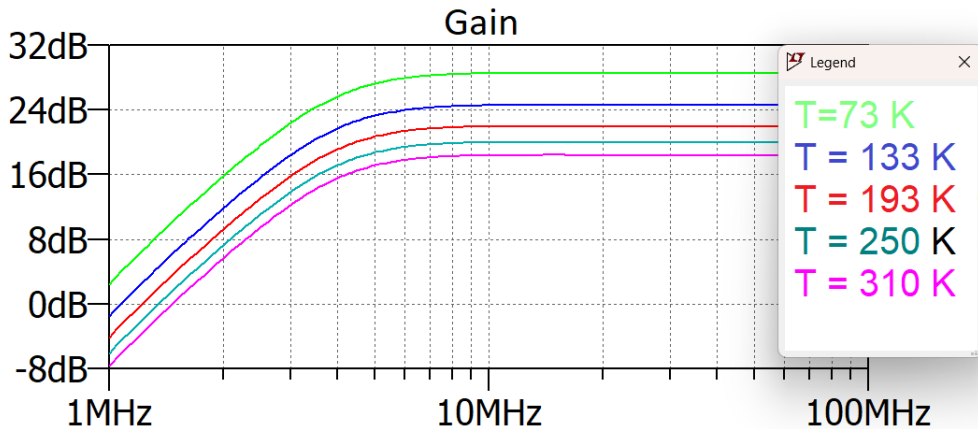


Figure 4.6: Voltage gain  $V_{out}/V_{in}$  for various temperatures in Kelvins. Amplification rises with decreasing temperature. The gain was increased by 10 between temperatures  $T = 310$  K and  $T = 73$  K.

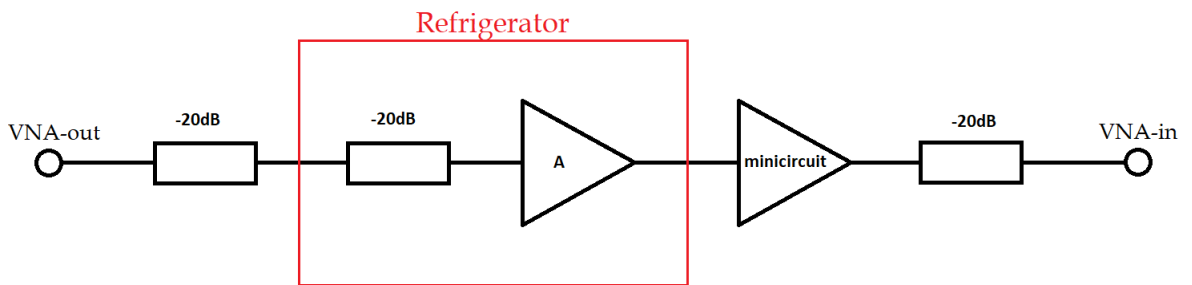


Figure 4.7: Schematic illustration of amplification measurements. Measurements have been carried out on the VNA.

temperature and frequency 30MHz the value was  $0.9 - 1 \text{ nV}/\sqrt{\text{Hz}}$ , which corresponds to the thermal noise of the  $50\Omega$  resistor. The measured noise at the room temperature (Fig.4.12) was  $5 \text{ nV}/\sqrt{\text{Hz}}$ , which shows that the amplifier noise dominates. Cooling the temperature down the amplifier noise rapidly decreases to the value  $0.7 \text{ nV}/\sqrt{\text{Hz}}$ .

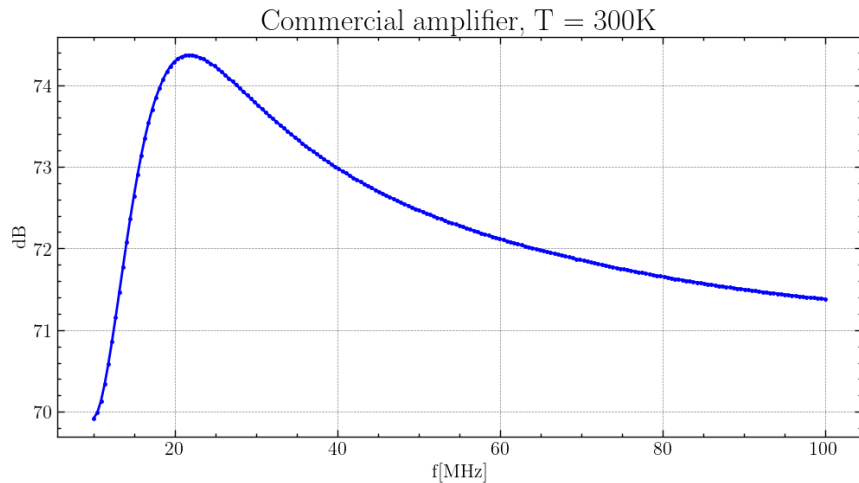


Figure 4.8: Amplification measurement in decibels for frequency spectrum, of the commercial amplifier at room temperature.

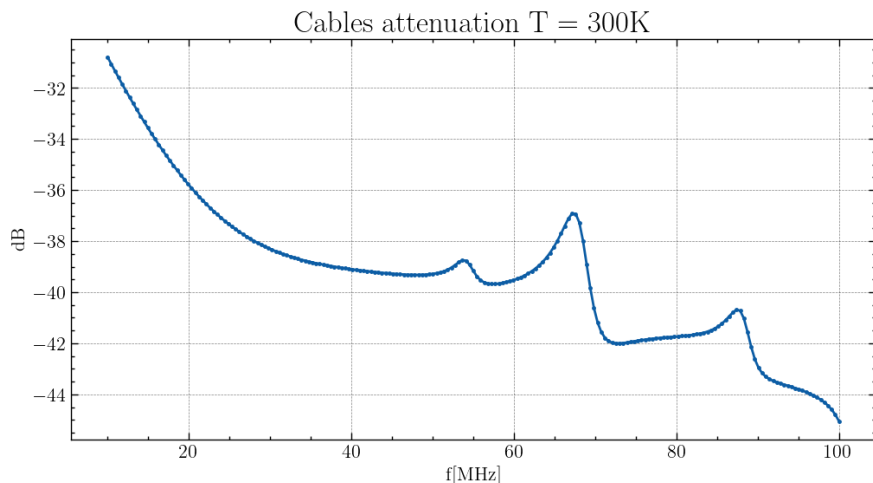


Figure 4.9: Refrigerator cables attenuation in decibels for frequency spectrum on room temperature  $T = 300$  K

### 4.3 Tank Circuit

We have used non-contact measurements to measure superconducting currents. A parallel RLC tank circuit, shown in Fig.4.13, is inductively coupled to a superconducting structure which leads to a shift unloaded resonance frequency  $\omega_0$  to the effective resonance frequency  $\omega_{eff}$ , related to the effective inductance  $L_{eff}$ .

Transmission measurement of a tank circuit can be done by Vector Network Analyser (VNA). The displayed transition on VNA will be a resonant peak. Theoretical transmission dependence is the impedance amplitude of the tank circuit. A complex impedance for the coupled tank circuit will be:

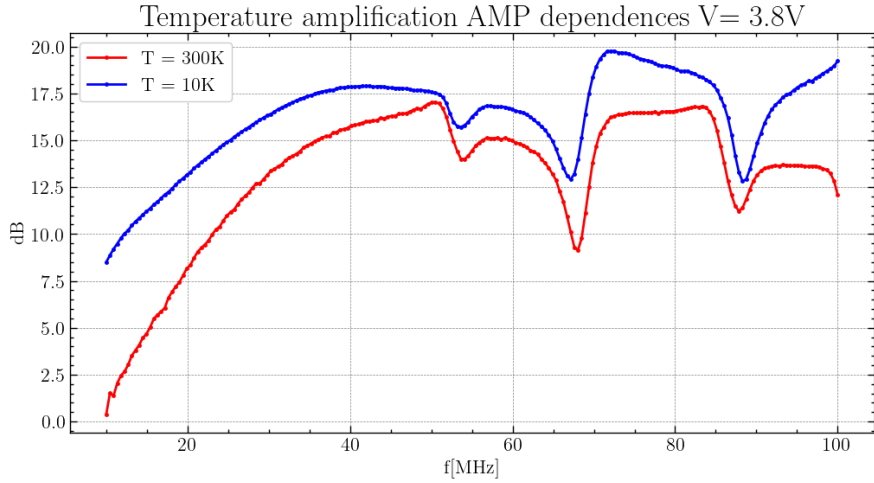


Figure 4.10: Amplification comparison for room temperature  $T = 300$  K and low temperature  $T = 10$  K.

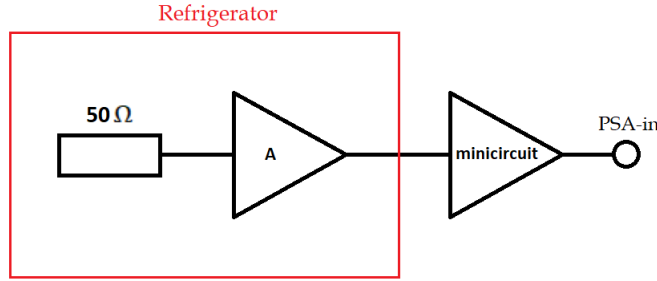


Figure 4.11: Measuring Setup for noise measurements on PSA: As noise generator, the  $50\ \Omega$  attenuator has been used.

$$Z(i\omega) = \frac{1}{\sqrt{R + \frac{1}{i\omega L_{eff}} + i\omega C}} \quad (4.14)$$

$$= \frac{1}{\sqrt{R + \frac{1}{\omega L_{eff}^2} \left( \frac{\omega^2}{\omega_{eff}^2} - 1 \right)}} \quad (4.15)$$

Where  $i$  is the imaginary number,  $\omega$  is the angular frequency. As we can see in Fig.4.15, the frequency characteristic has a Lorentzian shape. The maximum impedance is at the resonance frequency. The width of the resonance peak is given by the quality factor  $Q$ , which is defined as the ratio of power stored in the circuit over dissipated power

$$Q = \frac{P_{stored}}{P_{diss}} = \frac{X_L}{X_R} = \frac{X_C}{X_R}, \quad (4.16)$$

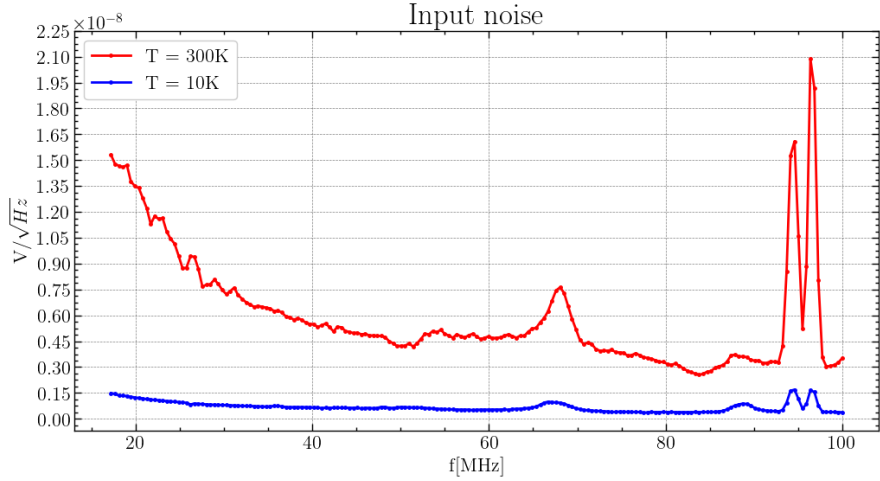


Figure 4.12: Input noise measurement results. Achieving  $T = 10$  K the noise is 10 times suppressed.

where  $X_L$ ,  $X_C$ ,  $X_R$  are the inductance, conductance, and reactance of a tank circuit. Another equal definition of quality factor is the ratio of resonance frequency  $\omega_0$  and bandwidth  $\Delta f$ , where bandwidth is defined as the difference of two frequencies at the -3 dB power level from the maximum

$$Q = \frac{\omega_0}{\Delta f} = \frac{\omega_0}{f_{2,-3dB} - f_{1,-3dB}}. \quad (4.17)$$

### 4.3.1 Design And Test

The tank circuit was connected to an RC-mixer. For the construction was manufactured custom box, see Fig.4.13. RC-mixer was soldered using scheme Fig.4.14. The upper body of the device with RC-mixer is connected to the tank circuit via a superconducting coaxial cable of length  $\approx 1\text{cm}$ . The whole device was put into the copper shell with lead shielding thermally anchored to the 300 mK plate. The shielding was implemented by putting lead solder on the outer surface of the copper shell. The thickness of the lead layer is  $\approx 1\text{mm}$ . The complete composition of the RC-mixer and tank circuit was simulated in LT-SPICE showing a quality increase with temperature decrease. For values  $L_T = 12.5\text{ nH}$  and  $C = 2\text{ nF}$  used in the circuit, the simulation resonance frequency was  $\omega_0 = 31.7\text{ MHz}$  and quality factor  $Q = 158.5$ .

### The Tank Circuit Measurement

For the test measurement, we have chosen a COILCRAFT inductor with inductance  $L_T = 12.5\text{ nH}$  and two parallel capacitors with  $C = 1\text{ nF}$ . Measurements were realized at the room temperature  $T_r = 300\text{ K}$ . The transmission has been measured for constellation RC-mixer + tank circuit + amplifier. Measurement has been also carried out on two voltages  $V_1 = 2\text{ V}$  and  $V_2 = 3\text{ V}$  with added capacitor on the tank circuit output.

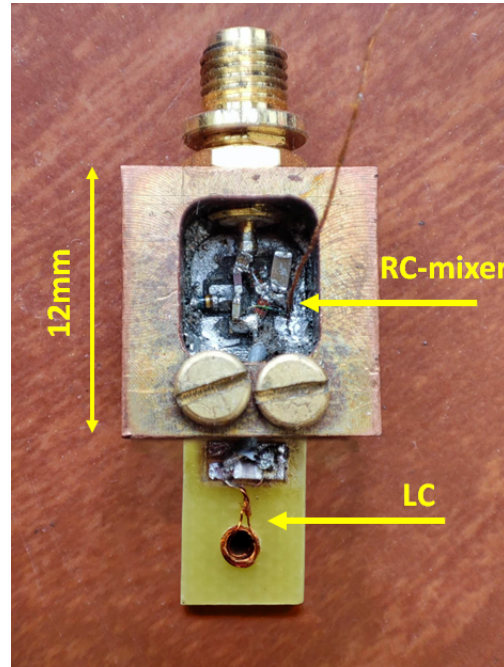


Figure 4.13: RC-mixer is soldered on PCB 7.5 mm wide and 10.5 mm and is thermally connected to the copper box inner surface. The tank circuit is soldered to the extended PCB which will be covered with a copper box shield.

## Results

The measured resonance frequency was  $\omega_0 = 26.4$  MHz, which is less than the theoretical value 31.7 MHz. This difference could be caused by neglecting the capacity, inductivity, and resistance of the real wires in the simulation. This also caused a big quality factor difference between measured and simulated values. The highest achieved quality factor value we measured (Fig.4.17) was  $Q = 38$ , while the simulated (Fig.4.15 one was  $Q = 158.8$ .

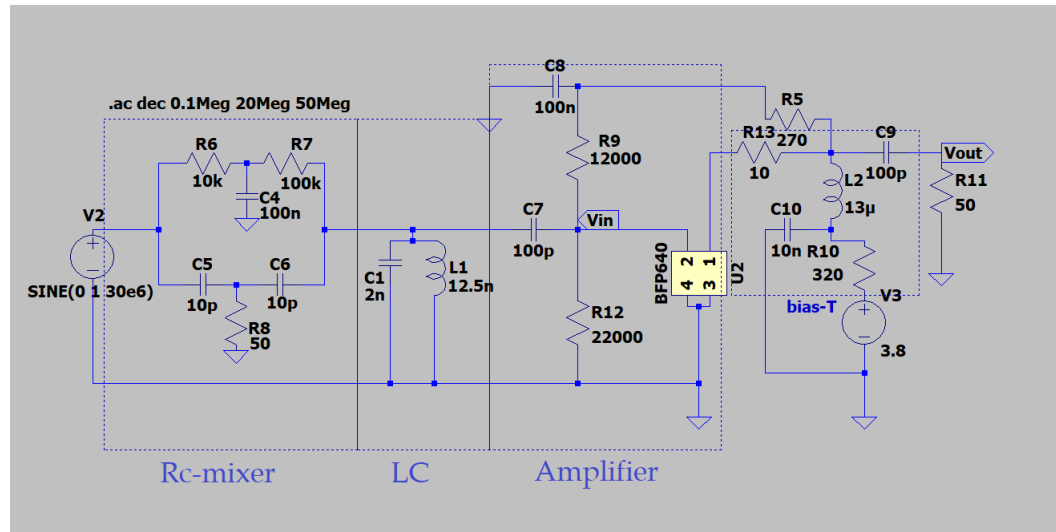


Figure 4.14: Simulation of the complete measurement circuit. RC-mixer and LC circuit will be placed on a 300 mK refrigerator plate. Bias-T protects the DC source from AC signals, it will be placed at room temperature.

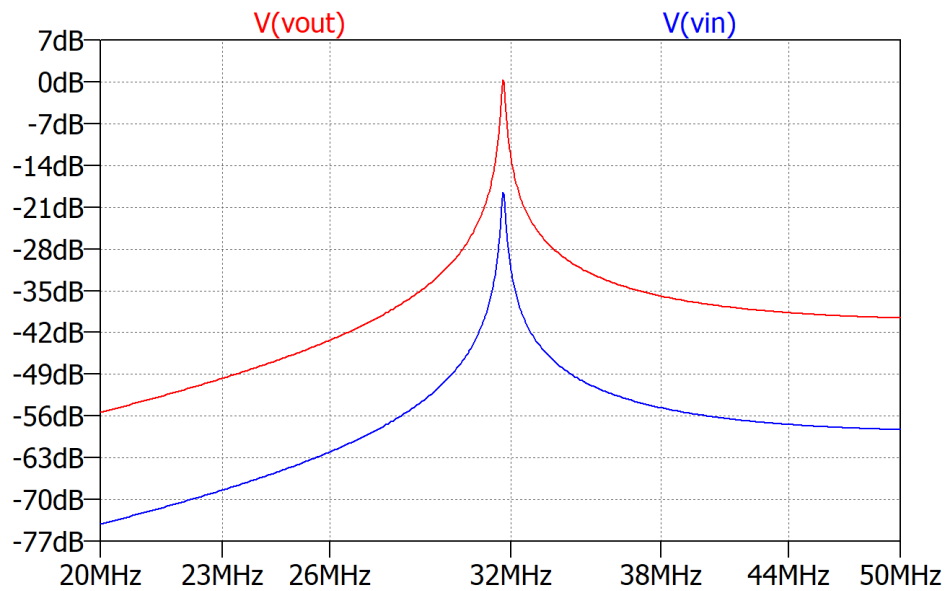


Figure 4.15: Simulation of LC tank circuit in decibels with  $L_T = 12.5 \text{ nH}$  and  $C_T = 2 \text{ nF}$  with theoretical resonance frequency  $\omega_r = \approx 32 \text{ MHz}$ . The curve has a Lorentzian shape.

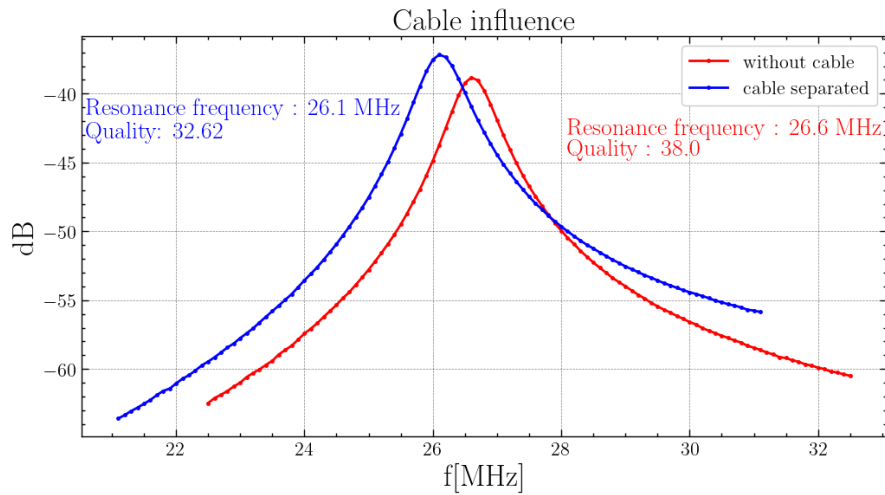


Figure 4.16: Measured influence of separating LC with coaxial cable. Cable impedance lowers the circuit quality.

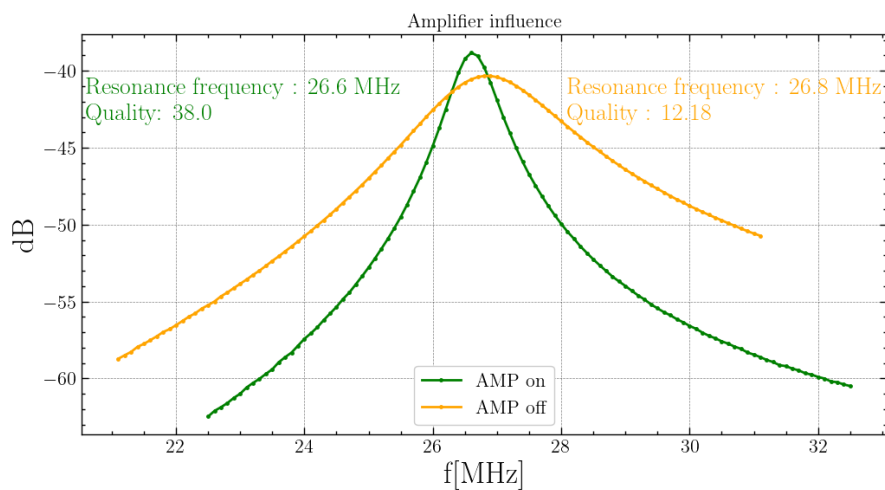


Figure 4.17: Measured amplifier influence on LC quality and resonance frequency. Turning the amplifier off there is a quality drop from value  $Q = 38$  to  $Q = 12.18$ , which can be also seen from resonance peak expansion.

# Chapter 5

## rf-SQUID measurement

In this chapter, we will provide the theoretical foundation for measuring the current-phase characteristics of a Josephson junction. We will also present the measurements of NbN nanobridges using the apparatus described in the preceding chapters.

### 5.1 Current-phase measurement

The current-phase relationship can be measured by an RLC tank circuit magnetically coupled to a superconducting loop containing a weak link. The Eq.3.11 can be written in the form

$$\varphi = \varphi_e - \beta i(\varphi), \quad (5.1)$$

where  $\varphi_e = 2\pi\Phi_e/\Phi_0$  is external magnetic flux provided by the coil of the tank circuit,  $\beta = 2\pi \frac{LI_C}{\Phi_0}$  is normalized inductance of the superconducting loop, and  $i(\varphi) = I_S/I_C$  is normalized super-current of the Josephson junction with critical current  $I_C$ .

The voltage across the tank circuit with the inductance  $L_T$  is influenced by the superconducting current  $I_S$  flowing through the superconducting loop

$$V_T = L_T \frac{dI_T}{dt} - M \frac{dI_S(\varphi)}{dt}, \quad (5.2)$$

where  $M = k\sqrt{LL_T}$  is mutual inductance between the superconducting loop and tank circuit characterized by coupling coefficient  $k$ . One can define an effective inductance  $L_{eff}$ :

$$L_{eff} = L_T - \frac{2\pi M^2}{\Phi_0} \frac{I'_S(\varphi)}{1 + \frac{2\pi L}{\Phi_0} I'(\varphi)}, \quad (5.3)$$

and rewrite Eq. ?? in the form

$$V_T = L_{eff} \frac{dI_T}{dt}. \quad (5.4)$$

The effective inductance change of the tank circuit resonance frequency from  $\omega_0 = 1/\sqrt{L_T C_T}$  to  $\omega_r = 1/\sqrt{L_{eff} C_T}$ . Now it is convenient to introduce normalized resonance frequency  $\tilde{\omega}_r = \omega_r/\omega_0$  and detuning parameter

$$\Delta\tilde{\omega}_r = \frac{\omega_0 - \omega_r}{\omega_0} = \frac{1}{2} \frac{k^2 \beta i'(\varphi)}{1 + \beta i'(\varphi)}, \quad (5.5)$$

and express the well-known phase shift  $\Theta$  between the driving current and voltage  $V_T$  across the tank circuit with high quality factor  $Q \gg 1$  in the form [17]

$$\tan(\Theta) \approx 2\Delta\tilde{\omega}_r Q. \quad (5.6)$$

The phase shift  $\Theta$  can be measured by a phase-sensitive lock-in amplifier. Using expression  $d\varphi_e/d\varphi = 1 + di(\varphi_e)/d\varphi$  and Eqs. 5.5, Eq. 5.6 we obtain a differential equation

$$\frac{di(\varphi)}{d\varphi} = \frac{1}{k^2 \beta Q} \tan(\Theta(\varphi_e)). \quad (5.7)$$

In the experiment, we can set the phase  $\varphi_e$  by a dc current  $I_{dc}$  and small radio-frequency driving current  $I_{rf}$ . From the equation 5.7 we obtain relation

$$i(\varphi_{dc}) = \frac{1}{k^2 \beta Q} \int_0^{\varphi_{dc}} \tan(\Theta(\varphi_e)) d\varphi_e, \quad (5.8)$$

where all quantities can be determined from the experiment. Using Eq. 5.1 and  $i(\varphi_{dc})$  we can calculate current-phase relationship  $i(\varphi)$ .

## 5.2 NbN rf-SQUID current-phase characteristics

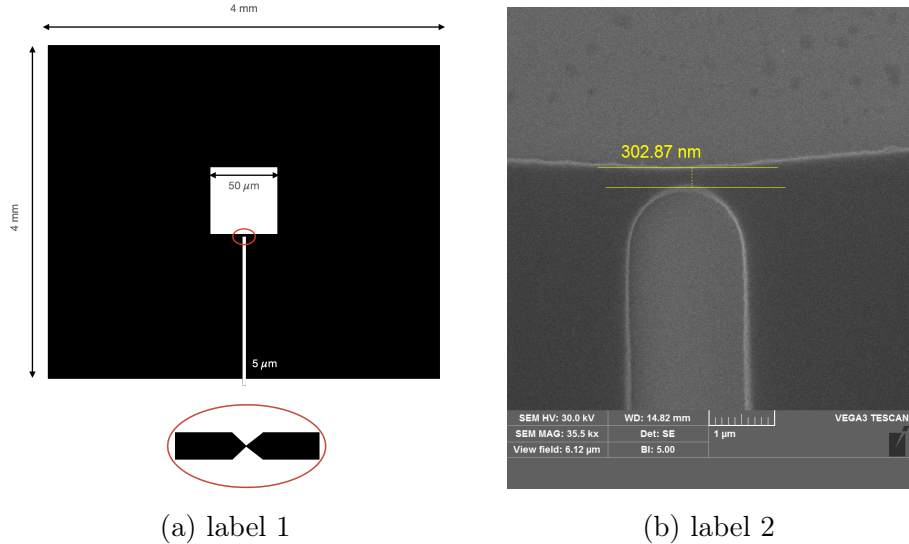
For measurement, we have used tank inductance  $L_T = 412$  nH which was measured by a tank circuit resonance at room temperature. The inductance of the superconducting loop  $L = 78$  pH was calculated from Ketchen formula considering the square washer geometry of rf-SQUID [26]

$$L = 1.25 \mu_0 d, \quad (5.9)$$

where  $\mu_0$  is permeability of the free space and  $d = 50$   $\mu\text{m}$  is the inner hole dimension (see Fig.5.1).

The coupling coefficient  $k$  between these two inductances can be determined from the SQUID periodicity [17] [18]

$$\Phi_0 = M \Delta I, \quad (5.10)$$



(a) label 1

(b) label 2

Figure 5.1: NbN rf-SQUIDs have been prepared by RNDr. Vladimír Tkáč, PhD. in UPJŠ Košice. (a)The geometry of NbN junction. rf - SQUID is a square-shaped loop with junction  $5 \mu\text{m}$  long. The superconducting current should flow in a  $\lambda$  depth of the inner cycle. (b)SEM photo of the NbN S-c-S Josephson junction. The junctions in the form of constriction are patterned by electron lithography as a 302.9 nm wide nanobridge.

where  $\Delta I$  is a current corresponding to the period. Hence the coupling coefficient  $k$  reads

$$k = \frac{M}{\sqrt{LL_T}} = \frac{\Phi_0}{\Delta I \sqrt{LL_T}}. \quad (5.11)$$

Substituting  $k$  into the relation for the superconducting current we get

$$I_S(\varphi_{dc}) = \frac{I_c}{\frac{\Phi_0^2}{\Delta I^2 LL_T} Q \beta} \int_0^{\varphi_{dc}} \tan(\Theta(\varphi_{dc})) d\varphi_{dc} \quad (5.12)$$

$$= \frac{\Delta I^2 L_T}{2\pi\Phi_0 Q} \int_0^{\varphi_{dc}} \tan(\Theta(\varphi_e)) d\varphi_e. \quad (5.13)$$

### 5.3 Measurement

To generate external magnetic flux, we have used two ac-voltage function generators. The first one generated a low-frequency triangular signal with frequency  $f = 3$  Hz with  $300 \text{ mV}_{pp}$  amplitude, which can be considered as a dc, and the second one generated a signal with high radio-frequency  $f = 42.2 \text{ MHz}$  with  $200 \text{ mV}_{pp}$  amplitude, as the rf-biasing part. The signals were mixed and directed to the refrigerator, passing through RC filters, a tank circuit, and a series of amplifiers - a primary low noise amplifier (BJT Si-Ge transistor) with gain +20 dB in the refrigerator thermally anchored

to plate with temperature  $T = 3$  K, and the secondary amplifier STANFORD with gain  $2 \times 12$  dB, on the room temperature.

For phase measurement, we have used a Lock-in amplifier which was set to give the phase as an analog output. Data were acquired by an oscilloscope, displaying an original triangular signal corresponding to dc magnetic flux  $\phi_{dc}$  and the phase  $\Theta$  from the Lock-in amplifier, as we can see in Fig.5.2.

The experimental setup shown in Fig.5.2 involves the generation and measurement devices: two AC voltage function generators, amplifiers, filters, and a lock-in amplifier. The first AC voltage function generator generates a low-frequency triangular signal with a frequency of  $f = 3$  Hz and an amplitude of  $300, \text{mV}_{\text{pp}}$ . This signal serves for the generation of the DC magnetic flux.

The second AC voltage function generator generates a high radio-frequency signal with a frequency of  $f = 42.2$  MHz and an amplitude of  $200, \text{mV}_{\text{pp}}$ . This signal serves for the generation of RF magnetic flux.

These two signals are mixed and directed to the refrigerator, passing through RC filters into the tank circuit. Both the RC filters and tank circuit help suppress electric noise. The signal from the tank circuit is then amplified using a series of amplifiers. The first amplifier is a low-noise amplifier based on a BJT Si-Ge transistor with a gain of  $+20$  dB. This amplifier is located in the refrigerator and is thermally anchored to a plate at a temperature of  $T = 3$  K, which ensures low noise operation in the cryogenic environment.

The signal is further amplified by a secondary STANFORD amplifier with a gain of  $2 \times 12$  dB. This amplifier is situated at room temperature.

For phase measurement, a lock-in amplifier is employed. The lock-in amplifier is configured to provide the phase as an analog output. It receives the amplified signal and extracts the desired phase information, which corresponds to the magnetic flux. Data acquisition is performed using an oscilloscope. The oscilloscope displays the original triangular signal corresponding to the DC magnetic flux  $\phi_{dc}$  and the phase  $\Theta$  obtained from the lock-in amplifier. This allows for visualizing and analyzing the measured data.

By changing the amplitude of the dc triangular signal, the period of rf-SQUID oscillations has been observed. Ten periods have been taken at different times and averaged to one plot shown in Fig.5.3.

## 5.4 Data analysis

After averaging the data had to be prepared for current-phase relationship calculation. The raw curve shown in Fig.(5.3) had been cut to interval from the first maximum

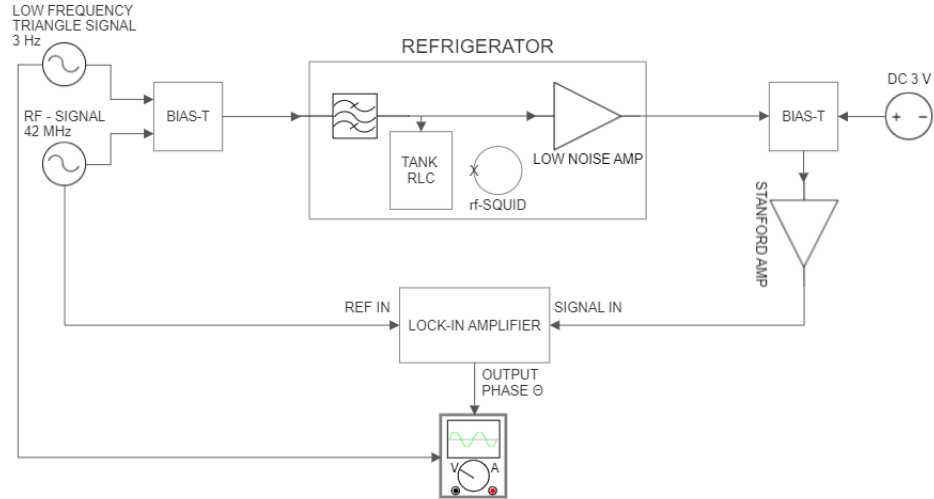


Figure 5.2: Schematics of current-phase measurement apparatus. There are three temperature stages of the refrigerator. The low-temperature amplifier is placed on the middle stage with temperature  $T = 3$  K. The RC mixer and the sample were placed on the lowest plate. The lowest plate has an adjustable temperature in the range of 300 mK to 3 K, allowing for control over the temperature at which the measurement is performed. The measurement has been done at the temperature  $T=3$  K.

to the last maximum of a measured sine wave, in the region where the triangle wave was linear. After that, we got five cosine periods on which the data were separated and shifted to zero value on the x-axis to overlap (Fig. (5.4)). Curves were averaged and symmetrized by mirroring the curve around the minimum value. Using symmetrization we have got one curve, which has been used for the calculation of the current-phase relationship.

Data taken from the oscilloscope were in volts. The phase in radians is obtained by multiplying the data by constant  $\pi/10$  V. The constant phase shift  $\Theta_0$  of the RF signal passing through cables and components can be determined from the condition  $\int_0^{2\pi} \tan(\Theta(\varphi_{dc})) d\varphi_{dc} = 0$ .

## 5.5 Experimental results

We have observed the predicted periodic dependence of phase shift between the dc current and biasing voltage of the tank circuit on the magnetic field. The period of oscillations observed on the oscilloscope changes with the slope of the dc current as predicted.

We have calculated the current as a function of the gauge invariant phase across the Josephson junction. From the known inductance of the rf-SQUID,  $L = 78$  pH, and

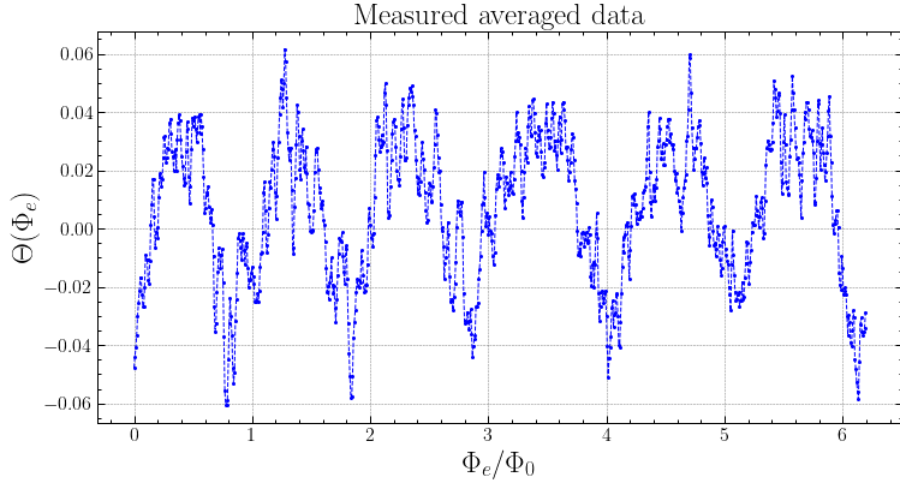


Figure 5.3: The bias voltage and current phase difference  $\Theta$  - phase  $\varphi$  dependence. Raw phase data from 10 frames of phase measurement were averaged and plotted.

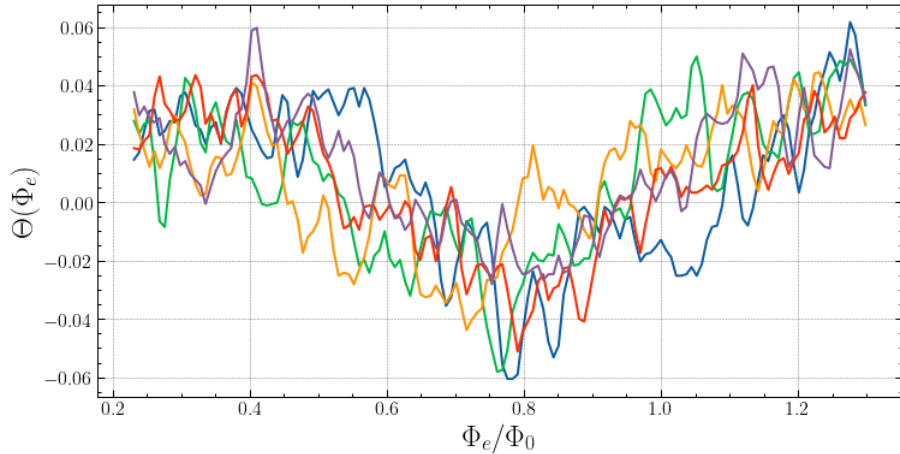


Figure 5.4: The five periods of the the measured  $\Theta(\varphi_{dc})$  dependence were extracted and averaged.

measured parameter  $\beta = 2\pi L I_C / \Phi_0 = 0.02 \ll 1$ , the critical current has been calculated to be  $I_C \approx 90$  nA. Thus the rf-SQUID is in the non-hysteretic regime, which can be also seen from the measured phase on Fig.5.6 - the phase shift has an almost perfect linear dependence on the  $\varphi_e$ .

Measured data shows the  $2\pi$  sinusoidal character of a superconducting current. As can be seen, the measured dependence is influenced by some interference. This cab is caused by weak sample shielding and strong interference of refrigerator power electronics. We have found strong interference at a frequency of 3 Hz coming from the compressor. As a protection a thin lead layer has been soldered on the top surface of the shielding shell, however, it has a lot of non-homogeneities, which could let magnetic field from the surrounding induce currents on the tank circuit.

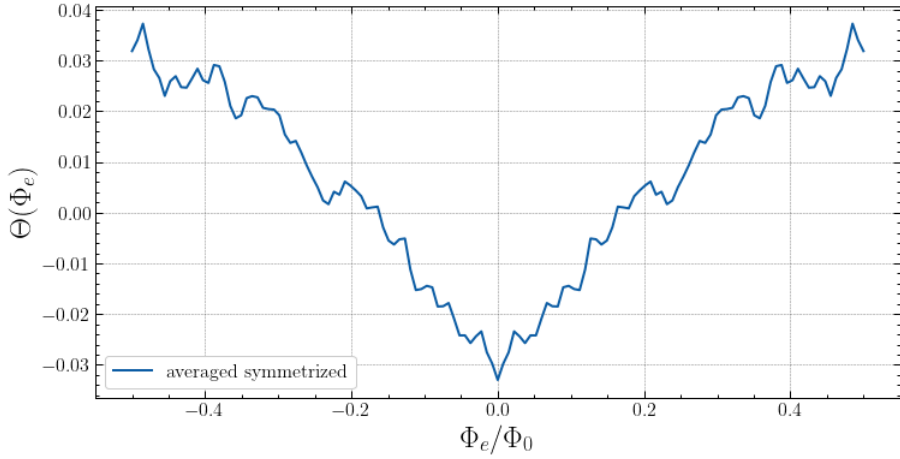


Figure 5.5:  $\Theta(\varphi_{dc})$  dependence. The averaged curve was mirrored over the minimum value and then averaged.

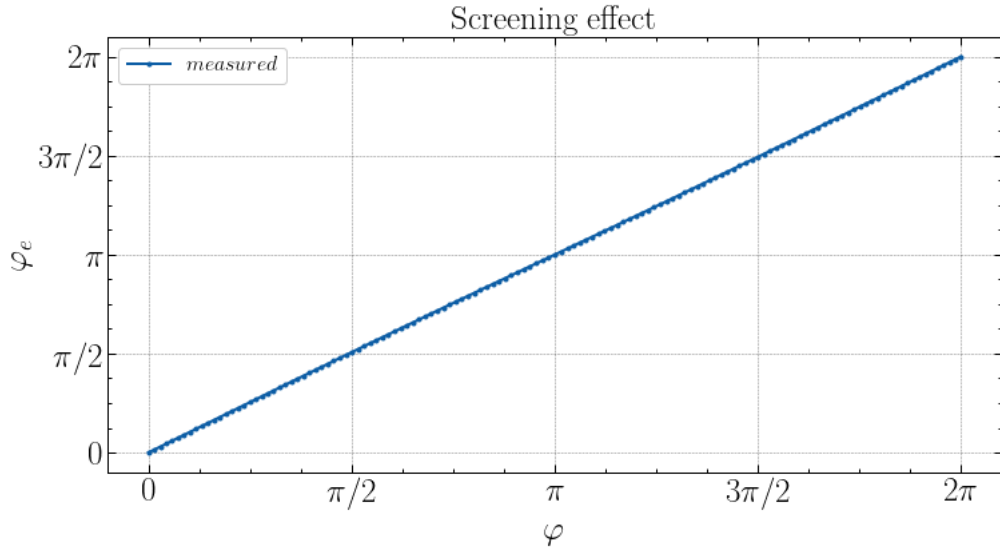


Figure 5.6: The screening effect  $\varphi_e(\varphi)$  external magnetic flux - phase dependence. Dependence is linear, which agrees with the theory for  $\beta \ll 1$ .

The experimental current-phase data have been firstly fitted using the current phase relationship for short clean junctions derived in Chapter 1,

$$I_S(\varphi) = e\tau\Delta/2\hbar \sin(\varphi)/\sqrt{1 - \tau \sin^2(\varphi/2)}.$$

The data can be fitted but with a physically unrealistic number of transition channels  $N \approx 3$  and too low value of the superconducting energy gap (Fig.5.7) of the junction  $\Delta_3 = 0.5$  meV. A more realistic model is the Kulik-Omelyanchuk 1 valid for the dirty short nanobridges (Fig.5.8). The energy gap can be determined from the fitted parameter to be  $\Delta_{KO-1} = 0.76$  meV.

Although the KO-1 model is closer to reality, the short limit should not apply to the NbN Dayem nanobridge. NbN has a very short mean free path compared to the coher-

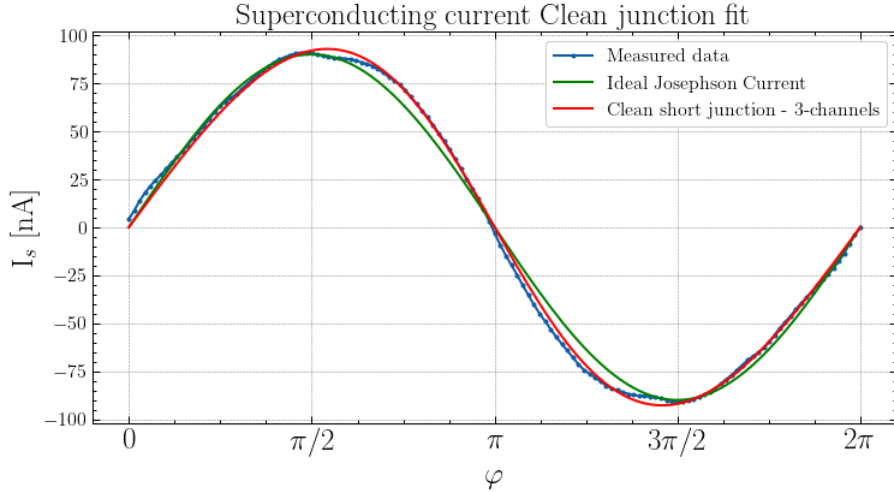


Figure 5.7: Current-phase characteristic. Using equation (5.13), we have computed integral super-current  $I_S$  with measured critical current  $I_C = 90.1$  nA and phases  $\varphi$  belonging to its values using  $\varphi = \varphi_{dc} - \beta i_S(\varphi_{dc})$ . The red curve is fit using the clean short junction limit for three transition channels. Fit was realized by the least square method with two fitting parameters  $K = \tau e \Delta / 2\hbar = 8.2 \times 10^{-23}$  and  $D = \tau = 0.41$ , where we have considered  $T \rightarrow 0$ , thus the  $\tanh(\sim 1/T) \rightarrow 1$ .

ence length [30]. According to [14] the mean free path  $l \approx 3$  Å and the Fermi velocity  $v_F \approx 1.5 \times 10^6$  m/s. The BCS coherence length can be estimated from the definition to be  $\xi_0 = 0.4$  nm. Considering the manufacturing process and the NbN coherence length it is more likely that the junction is in dirty long junction limit.

Nevertheless, one cannot exclude that in the narrowest section of the nanobridge, even narrower constriction can be formed.

The hexagonal and cubic NbN critical temperature has been measured to be  $T_C \approx 11.6$  K according to [46] [37], however, the disorder in the junction lower the value of the critical temperature. If the Dayem bridge is in the dirty long junction limit the measured dependence slightly tilted from the ideal sinus may mean that we were close to the critical temperature even on  $T \approx 3$  K. Considering the measured energy gap not to vary with temperature we can estimate the critical temperature to be  $T_C = \Delta_{KO-1} / 1.764 k_B \approx 5$  K, thus a half from the predicted value.

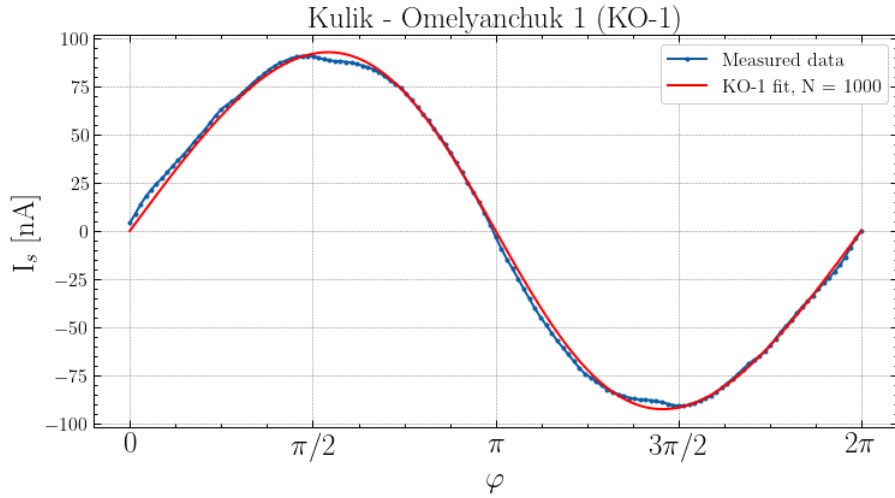


Figure 5.8: KO-1 fit. Using the dirty limit we get almost the same curve as in the clean short junction model for three channels. Fitting function was summing functions  $K_2 K_1 \cos(\varphi/2)/\delta \arctan(K_1 \sin(\varphi/2)/\delta)$  for  $N=1000$  Matsubara frequencies. The final values of fitting parameters are  $K_1 = \Delta = 0.76$  meV,  $K_2 = 2\pi k_B T/eR_N = 2.9 \times 10^{-7}$

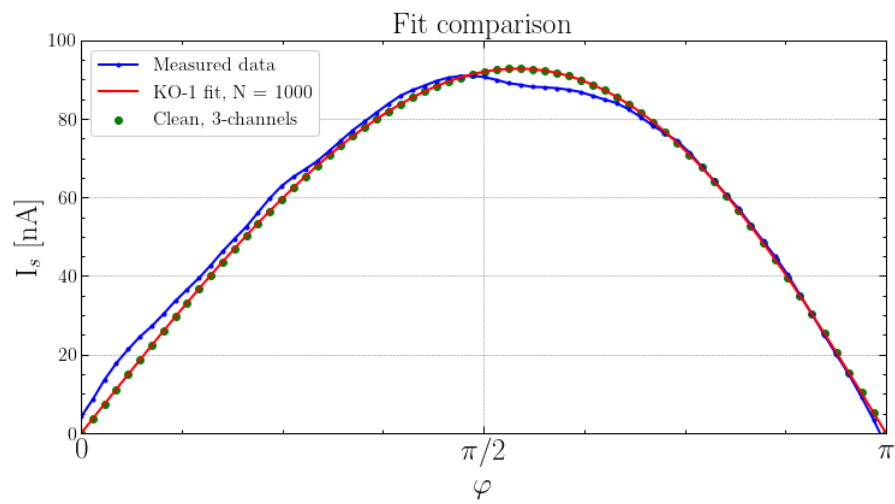


Figure 5.9: Comparison of current-phase characteristics  $I_S(\varphi)$  in the half period interval  $(0, \pi)$  for used models: clean short junction limit - green dots and dirty short junction limit KO-1 - red line, with measured data - blue dotted line.

# Chapter 6

## Conclusion

The main goal of this work was to measure the current-phase characteristic of a Josephson junction. We designed an apparatus that was constructed and tested. With the apparatus, we were able to measure the current-phase characteristic of an NbN rf-SQUID, which proved to be functional. The measurements showed that the current-phase relationship is slightly tilted compared to the sinusoidal one. Therefore, we applied a model to describe a clean short junction and a dirty short junction KO-1. Both models are able to fit the measured data but with different fitting parameters. The energy gap evaluated from the KO-1 model is  $\Delta = 0.76$  meV, for which we evaluated the critical temperature of the junction  $T_C = 5$  K, the coherence length  $\xi_0 = 0.4$  nm, and the normal resistance  $R_N = 8.9 \times 10^{-5} \Omega$ . Comparing the coherence length with the mean free path for NbN,  $l \approx 3 \text{ \AA}$  [14], it is evident that the rf-SQUID is at the limit of a dirty junction. Despite the problem of precisely determining the effective junction length  $L_{eff}$  due to its shape, a comparison of the approximate bridge length  $L \approx 1 \mu\text{m}$  with the coherence length  $\xi_0$  suggests a long bridge limit. However, this limit should lead to hysteretic behavior which has not been observed. During the measurement, we encountered problems with strong noise from refrigerator and surroundings. We temporarily tried to solve the noise problem by applying a lead layer soldered onto the copper box. This solution proved to be unreliable, so we plan to change it in the future. One suggestion is to pour lead into the inside of the lid or to use  $\mu$  metal for noise reduction. This improvement could help suppress the noise, leading to cleaner data and more accurate results. The device could also be improved by changing the overall design. Currently, it is challenging to replace damaged components. Therefore, we plan to design a new one that would be easier to maintain. One of the most significant obstacles to measurement was the quality of the LC circuit. We tried using various coils to achieve the highest quality, but we were unable to exceed  $Q = 100$ . High quality is necessary for the resolution of the resonance frequency deviation during measurement.

# Bibliography

- [1] Ltspice web page. <https://www.analog.com/en/design-center/design-tools-and-calculators/ltspice-simulator.html>.
- [2] Minicircuit amplifier datasheet. <https://www.minicircuits.com/pdfs/ZX60-33LN+.pdf>.
- [3] M. Yu. Kupriyanov A.A. Golubov and E. Il'ichev. The current-phase relation in josephson junctions. *Rev. Mod. Phys.*, 76(2):446–449, 2004.
- [4] Yau-Chuen Yam Aaron Kraft, Christoph Rupprecht. Superconducting quantum interference device (squid). *UBC PHYSICS*, 502, 2017.
- [5] Philip F. Bagwell. Suppression of the josephson current through a narrow, mesoscopic, semiconductor channel by a single impurity. *PHYSICAL REVIEW B*, 46(19), 1992.
- [6] N. H. Balshaw. *Practical Cryogenics: An Introduction to laboratory cryogenics*. Oxford Instruments, Scientific Research Division, 1996.
- [7] J. Bardeen, L. N. Cooper, and J. R. Schrieffer. Theory of superconductivity. *Phys. Rev.*, 108:1175–1204, Dec 1957.
- [8] M. R. Beasley. Notes on the ginzburg-landau theory. <http://www.icmr.ucsbs.edu/programs/documents/Beasley.pdf>, August 2009.
- [9] C. W. J Beenakker. Universal limit of critical-current fluctuations in mesoscopic josephson junctions. *PHYSICAL REVIEW LETTERS*, 67(27), 1991.
- [10] M. Belogolovskii, M. Grajcar, P. Kúš, A. Plecenik, Š. Beňačka, and P. Seidel. Phase-coherent charge transport in superconducting heterocontacts. *Physical Review B*, 59(14):9617–9626, 1999.
- [11] Daniel Bobok. *Prúdovo- fázové charakteristiky Josephsonových spojov na báze topologických materiálov*. Bachelor thesis, 2021.

- [12] Lennart Bours. *Superconductivity in topological edge states and gated Dayem Bridges*. Phd thesis, 2021.
- [13] J. A. Connely C. D. Motchenbacher. *Low-Noise Electronic System Design*. John Wiley Sons, Inc., New York, 1993.
- [14] S. P. Chockalingam, Madhavi Chand, John Jesudasan, Vikram Tripathi, and Pratap Raychaudhuri. Superconducting properties and hall effect of epitaxial NbN thin films. *Physical Review B*, 77(21), jun 2008.
- [15] Nicolas Didier. The josephson effect in superconductors and quantum gases, Feb 2010.
- [16] Fabrizio Dolcini. Andreev reflection lecture notes. <https://studylib.net/doc/18334553/andreev-reflection>, October 2009.
- [17] H.-G. Meyer et al. E. Il'ichev, H.E. Hoenig. Measurements of small supercurrents in niobium squid circuits. *Physica C*, 352:141 – 143, 2001.
- [18] L. Fritzsch et al. E. Il'ichev, V. Zakosarenko. Radio-frequency based monitoring of small supercurrents. *AIP Review of Scientific Instruments*, 72(3):1882–1887, 2001.
- [19] L. Fritzsch et al. E. Il'ichev, V. Zakosarenko. Radio-frequency based monitoring of small supercurrents. *AIP Review of Scientific Instruments*, 72(3):1882–1887, 2001.
- [20] Tomáš Fiantok. *Charakterizácia supravodivých materiálov vysokofrekvenčnými metódami*. Bachelor thesis, 2016.
- [21] Mark Fox. *Quantum Optics*. Oxford University Press Inc., 2006.
- [22] Sergey Maksimovich Frolov. *Current-phase relations of Josephson junctions with ferromagnetic barriers*. PhD thesis, 2005.
- [23] Roy Haller. *Probing the microwave response of novel Josephson elements*. Phd thesis, 2021.
- [24] Richard Hlubina. Fyzika mnohých častíc. [http://www.st.fmph.uniba.sk/~hlubina1/STUD\\_MATER/FMC/fmc.pdf](http://www.st.fmph.uniba.sk/~hlubina1/STUD_MATER/FMC/fmc.pdf), December 2020.
- [25] E. Il'ichev, H.E. Hoenig, H.-G. Meyer, A.B. Zorin, V.V. Khanin, M. Götz, A.B. Pavolotsky, and J. Niemeyer. Measurement of small supercurrents in niobium squid circuits. *Physica C: Superconductivity*, 352(1–4):141–143, 2001.
- [26] M.B. Ketchen. Integrated thin-film dc squid sensors. *IEE Transactions on magnetics*, MAG-23, no.2:1650 – 1657, 1987.

- [27] A Yu Kitaev. Unpaired majorana fermions in quantum wires. *Physics-Uspekhi*, 44(10S):131–136, 2001.
- [28] I.O. Kulik. Macroscopic quantization and the proximity effect in s-n-s junctions. *SOVIET PHYSICS JETP*, 30(5), 1969.
- [29] V. L. Lebedev. *Random Processes in Electrical and Mechanical Systems*. The State Publishing House of Physical and Mathematical Literature, Moscow, 1958.
- [30] K. K. Likharev. Superconducting weak links. *Reviews of Modern Physics*, 51(1), 1979.
- [31] Rodney Loudon. *The Quantum Theory of Light*. Oxford University Press Inc., 2001.
- [32] Michal Maheľ. *Analógové Systémy*. Fakulta matematiky, fyziky a informatiky UK Knižničné a edičné centrum, 2022.
- [33] Michal Maheľ. Magnetické vlastnosti tuhých látok učebný text. <http://davinci.fmph.uniba.sk/~mahel1/KOOP/>, 2023.
- [34] A. Mourachkine. Determination of the coherence length and the cooper-pair size in unconventional superconductors by tunneling spectroscopy. *Journal of Superconductivity*, 17:711–724, 2004.
- [35] Michael Martin Nieto. Quantum phase and quantum phase operators: Some physics and some history. [https://core.ac.uk/display/25351228?utm\\_source=pdf&utm\\_medium=banner&utm\\_campaign=pdf-decoration-v1](https://core.ac.uk/display/25351228?utm_source=pdf&utm_medium=banner&utm_campaign=pdf-decoration-v1), 1993.
- [36] Henry W. Ott. *Noise reduction techniques in electronic systems, Second Edition*. John Wiley Sons, Inc., United States of America, 1988.
- [37] V.M. Pan, V.P. Gorishnyak, E.M. Rudenko, V.E. Shaternik, M.V. Belous, S.A. Kozlychuk, and F.I. Korzhinsky. Investigation of the properties of superconducting niobium nitride films. *Cryogenics*, 23(5):258–262, 1983.
- [38] Frank Pobell. *Matter and methods at low temperatures*. Springer, 2007.
- [39] G. J. Podd, G. D. Hutchinson, D. A. Williams, and D. G. Hasko. Micro-squids with controllable asymmetry via hot-phonon controlled junctions. *Physical Review B*, 75(13), 2007.
- [40] Anna Posazhennikova. Josephson effect in superconductors and superfluids, 2009.

- [41] Mohammad A Rashid. Lecture notes: Superconductivity. [https://rashid-phy.github.io/me/pdf/notes/Superconductor\\_Theory.pdf](https://rashid-phy.github.io/me/pdf/notes/Superconductor_Theory.pdf), September 26 2019.
- [42] Masatoshi Sato and Satoshi Fujimoto. Majorana fermions and topology in superconductors. *Journal of the Physical Society of Japan*, 85(7):072001, 2016.
- [43] Carsten Timm. Notes on the ginzburg-landau theory. [https://tu-dresden.de/mn/physik/itp/cmt/ressourcen/dateien/skripte/Skript\\_Supra.pdf](https://tu-dresden.de/mn/physik/itp/cmt/ressourcen/dateien/skripte/Skript_Supra.pdf), March 24 2023.
- [44] Michael Tinkham. *Introduction to superconductivity: V. 1.* Dover Publications Inc, 2004.
- [45] J. Wiedenmann, E. Bocquillon, R. S. Deacon, S. Hartinger, O. Herrmann, T. M. Klapwijk, L. Maier, C. Ames, C. Brüne, C. Gould, and et al. 4-periodic josephson supercurrent in hgte-based topological josephson junctions, Jan 2016.
- [46] Yongtao Zou, Xintong Qi, Cheng Zhang, Shuailing Ma, Wei Zhang, Ying Li, Ting Chen, Xuebing Wang, Zhiqiang Chen, David Welch, and et al. Discovery of superconductivity in hard hexagonal -nbn. *Scientific Reports*, 6(1), 2016.